ACS NANO

www.acsnano.org

ARTICLE

Biaxial Tensile Strain Enhances Electron Mobility of Monolayer Transition Metal Dichalcogenides

Jerry A. Yang, Robert K. A. Bennett, Lauren Hoang, Zhepeng Zhang, Kamila J. Thompson, Antonios Michail, John Parthenios, Konstantinos Papagelis, Andrew J. Mannix, and Eric Pop*

Cite This: *ACS Nano* 2024, 18, 18151−18159

Read Online

ACCESS | Metrics & More | Article Recommendations | Supporting Information

ABSTRACT: **Strain engineering can modulate the properties of two-dimensional (2D) semiconductors for electronic and optoelectronic applications. Recent theory and experiments have found that uniaxial tensile strain can improve the electron mobility of monolayer MoS_2, a 2D semiconductor, but the effects of biaxial strain on charge transport are not well characterized in 2D semiconductors. Here, we use biaxial tensile strain on flexible substrates to probe electron transport in monolayer WS_2 and MoS_2 transistors. This approach experimentally achieves ~2× higher on-state current and mobility with ~0.3% applied biaxial strain in WS_2, the highest mobility improvement at the lowest strain reported to date. We also examine the mechanisms behind this improvement through density functional theory simulations, concluding that the enhancement is primarily due to reduced intervalley electron−phonon scattering. These results underscore the role of strain engineering in 2D semiconductors for flexible electronics, sensors, integrated circuits, and other optoelectronic applications.**

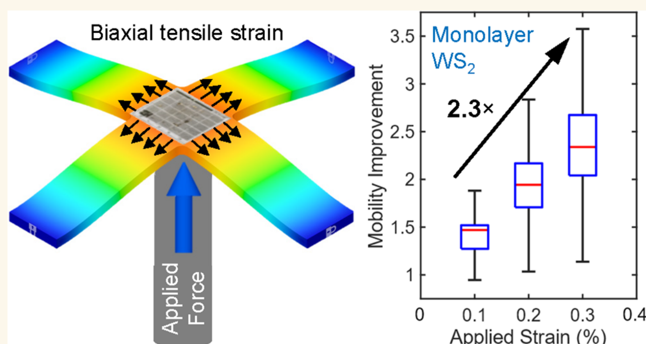

KEYWORDS: *2D materials, WS_2, MoS_2, transistors, biaxial strain, mobility*

Downloaded via STANFORD UNIV on July 28, 2024 at 00:29:46 (UTC).
See https://pubs.acs.org/sharingguidelines for options on how to legitimately share published articles.

Two-dimensional (2D) semiconductors have gained significant interest for electronic and optoelectronic devices due to their atomically thin structure,[1] theoretically pristine van der Waals interfaces,[1,2] and potential for heterogeneous integration into monolithic three-dimensional (3D) computing systems.[1,3] Tungsten disulfide, WS_2, and molybdenum disulfide, MoS_2, are commonly explored 2D transition metal dichalcogenide (TMD) semiconductors because they can be grown in single layers over large areas,[4−6] have good electron mobilities at atomic-scale thicknesses,[7] and may exhibit electronic ambipolarity as a single or multilayer material.[8,9] However, significant challenges remain in incorporating WS_2 and other TMDs into large-scale heterogeneous integration schemes, one of which is improving electrical performance metrics such as the mobility and on-state current of TMD-based field-effect transistors (FETs). While techniques including channel doping,[10] interface engineering,[11,12] and contact engineering[12] have been used to improve electrical performance of WS_2 transistors, the potential for strain engineering to enhance device performance remains to be explored.

Recently, an experimental study has shown that the mobility of monolayer MoS_2 is nearly doubled with less than 1% tensile strain,[13] while theoretical efforts have predicted effects of both tensile and compressive strain on the band structure[14,15] and mobility[16−18] of various TMDs. In particular, simulations show that biaxial strain should have a stronger effect on monolayer MoS_2 mobility compared to uniaxial strain.[19] The study of strain on transistor performance also has industrial relevance; for example, tensile and compressive strain are built into every modern silicon transistor to enhance the electron and hole mobilities, respectively.[20] However, despite significant efforts in understanding the influence of strain on optical emission,[21] the effect of strain on the electronic properties of WS_2 and MoS_2, particularly under nonuniform and nonuniaxial strain

Received: September 19, 2023
Revised: February 12, 2024
Accepted: February 15, 2024
Published: June 26, 2024

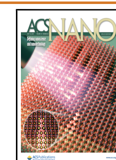

© 2024 American Chemical Society

https://doi.org/10.1021/acsnano.3c08996
ACS Nano 2024, 18, 18151−18159

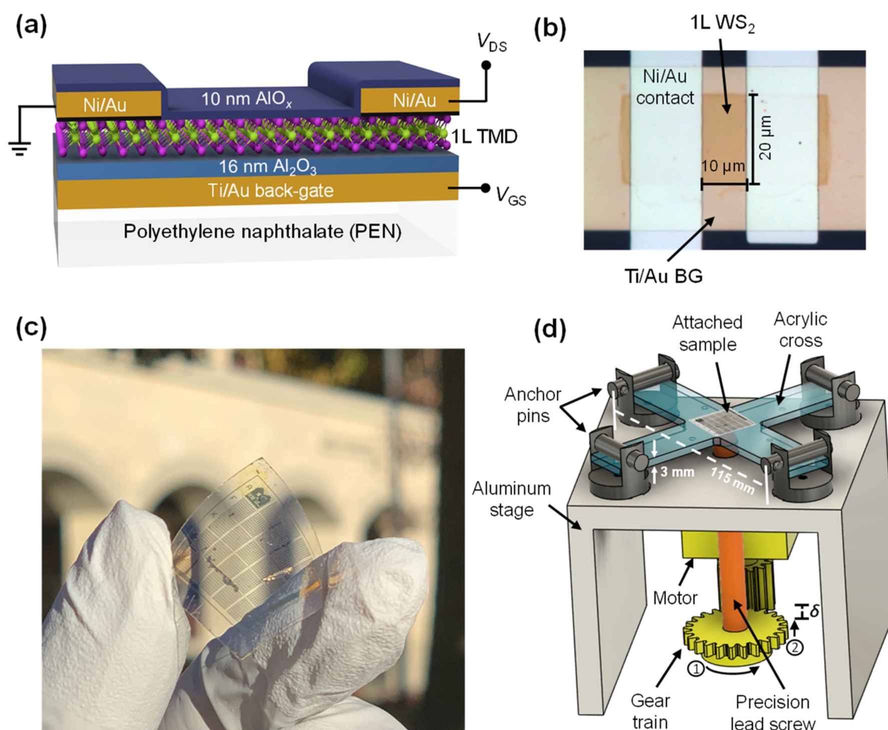

Figure 1. TMD device schematic and strain tool. (a) Schematic of back-gated (BG) monolayer (1L) WS_2 transistor on a polyethylene naphthalate (PEN) flexible substrate, with source and drain contacts (∼5 nm Ni capped with ∼40 nm Au), ∼16 nm thick Al_2O_3 back-gate dielectric, and ∼10 nm thick AlO_x encapsulation. (b) Top-view optical image of monolayer WS_2 transistor with channel width $W \approx 20$ μm, length $L \approx 10$ μm. (c) Photograph of flexed substrate chiplet with several hundred WS_2 devices. (d) Biaxial strain tool schematic. A motor drives a gear train, which turns a precision lead screw, deflecting the center of an acrylic cross, to which the sample is attached. The deflection imparts biaxial strain to the PEN sample.

fields, remains to be explored. In addition, theoretical studies have also predicted that WS_2 should have the highest intrinsic mobility and saturation velocity among the basic TMDs.[16,22]

In this work, we study the effect of biaxial tensile strain on the optical properties and electron mobility of alumina-encapsulated monolayer WS_2 and nonencapsulated monolayer MoS_2 transistors on bendable substrates. We find that the electron mobility and on-state transistor current increase by ∼100% at ∼0.3% biaxial tensile strain for WS_2 and ∼60% at the same strain for MoS_2. The encapsulation also significantly alters the optical band gap and Raman modes of WS_2 under tensile strain compared to nonencapsulated WS_2 films. We correlate our experimental results to density functional theory simulations for WS_2, confirming that the mobility and current enhancements likely result from reduced intervalley scattering rather than changes in electron effective mass. These results highlight that strain engineering can play a key role to improve the performance of TMD-based electronics.

RESULTS AND DISCUSSION

Device Structure and Biaxial Strain Tool Operation. Figure 1 shows the device structure of our TMD field-effect transistors fabricated on free-standing, flexible, and transparent substrates of poly(ethylene naphthalate) (PEN, 125 μm thick). Monolayer WS_2 and monolayer MoS_2 were grown on separate substrates, then transferred onto the PEN film, which had Al_2O_3 gate dielectrics on previously patterned metal back-gates (Figure 1a). The average grain size of the films is between 5 and 50 μm, which indicates that grain boundaries are not expected to dominate the resistance of our devices.[6] Ni/Au source and drain contacts were patterned on top by optical lithography and lift-off, and WS_2 devices were encapsulated by a thin layer of AlO_x. Figure 1b shows the top-down image of one finished device, and Figure 1c shows the flexible substrate with several hundred devices. Additional details regarding TMD growth and layer transfer are presented in the Methods section, the full fabrication process is discussed in Supporting Information Section 1, and the effect of the substoichiometric AlO_x on the electrical performance of WS_2 transistors is presented in Supporting Information Section 2.

We applied strain to our samples with a motorized stage shown in Figure 1d. (Also see Supporting Information Figure S2 for additional details.) An external Arduino microcontroller operates a precision lead screw that deflects an acrylic cross, to which the PEN sample is attached. The strain at the center of the cross can then be estimated as $\varepsilon \approx 4t\delta/D^2$, where $t = 3$ mm is the thickness of the acrylic cross, δ is the distance of deflection in millimeters, and $D = 115$ mm is the distance between two nonadjacent anchor pins. Previous modeling work has shown that this strain geometry produces a biaxial tensile strain field within 3 mm of the center, with the strain decaying to about 75% at 3 mm away from the center.[23] We note that due to the strong adhesion between the acrylic cross and the sample, as well as the low strain levels applied here (<1%), we expect nearly full strain transfer from the tool into the TMD devices without slippage, and we discuss this strain transfer efficiency in a forthcoming work.[24] Due to potential strain fields induced in the WS_2 from device fabrication and encapsulation, all strain measurements are reported relative to the as-fabricated devices after attachment to the acrylic cross and before loading onto the strain tool.

https://doi.org/10.1021/acsnano.3c08996
ACS Nano 2024, 18, 18151−18159

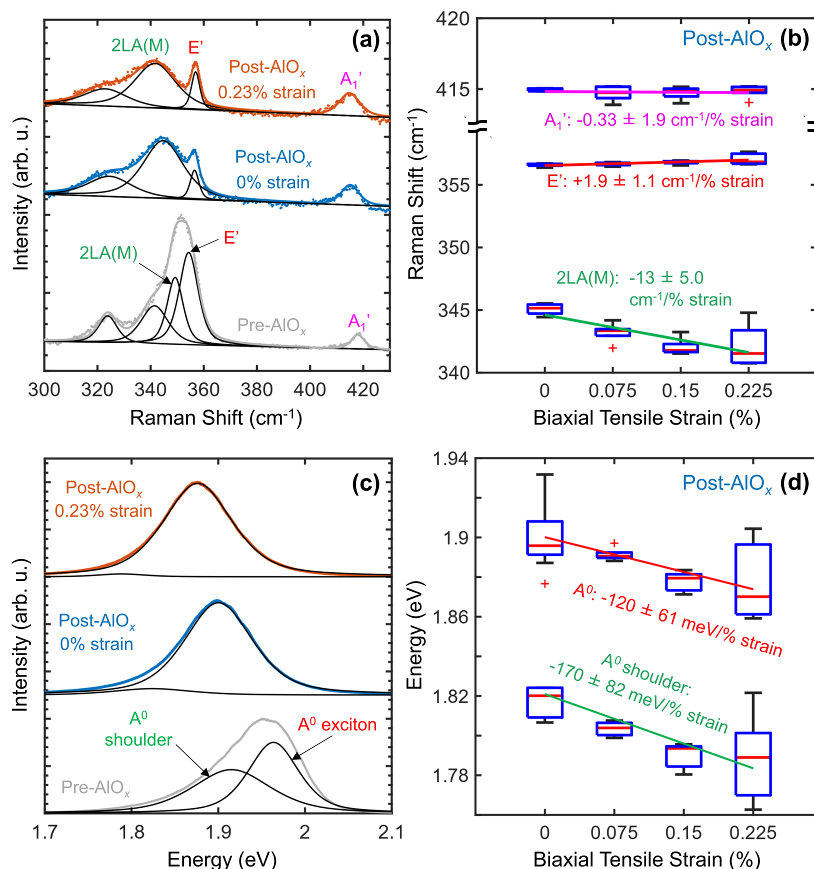

Figure 2. Raman and photoluminescence (PL) response of monolayer WS_2 to biaxial strain. (a) Raman spectra of a device with a similar geometry as in Figure 1b before encapsulation (gray), after AlO_x encapsulation (blue), and after AlO_x encapsulation with biaxial strain (orange). The data (symbols) are fitted with a superposition of Gaussian and Lorentzian peaks (black curves). (b) Estimated shift rates of the A_1' (pink), E' (red), and 2LA(M) (green) Raman peaks of the AlO_x-encapsulated WS_2 as a function of biaxial strain applied, with box plots indicating the median (red line) as well as first and third quartiles (blue box) across nine measured locations in the device channel. (c) PL spectra of the device at the same locations in the channel, under the same conditions and color labeling as in (a). (d) Extracted exciton shift rates of the A^0 exciton (red) and its left shoulder peak (green), with similar notation and the same number of points as in (b).

Spectroscopic Measurements of WS_2 Devices under Strain. We used Raman and photoluminescence (PL) spectroscopy to confirm strain transfer from the acrylic cross to the WS_2 devices (Figure 2). We monitor the positions of the A_1' peak at ~418 cm^{-1}, E' peak at ~356 cm^{-1}, 2LA(M) peak at ~348 cm^{-1}, A^0 exciton peak at ~1.95 eV, and the A^0 exciton shoulder peak at ~1.92 eV (usually assigned to the A^- trion[21,25]), respectively, as these peaks have been shown to be sensitive to strain.[21] We measure the spectra at nine points within the device channel for each strain level and then use linear regression to calculate the peak shift rate under strain for each peak.

Figure 2a shows the Raman spectra of a WS_2 device before encapsulation, after AlO_x encapsulation but before imparting strain, and after strain. Qualitatively, the AlO_x broadens the 2LA(M) peak and increases the prominence of the E' peak in the Raman spectrum, whereas the A_1' peak intensity remains unaffected. After encapsulation, the 2LA(M) and A_1' peaks redshift, while the E' peak slightly blueshifts. Figure 2b displays box plots of the Raman peak positions at each strain level and the estimated strain shift rate. Under strain, the 2LA(M) peak redshifts by 13 ± 5.0 cm^{-1}/% strain, and the E' peak blueshifts by 1.9 ± 1.1 cm^{-1}/% strain, whereas the A_1' peak does not appear to shift. The E' and A_1' peak shift rates in our encapsulated devices differ from previously reported strain rates of unencapsulated monolayer WS_2 under biaxial tensile strain,[21] likely because the AlO_x passivation step removes surface oxygen and water adsorbates,[26] inducing partial electron doping. (This is also seen as a negative threshold voltage shift in Supporting Information Figure S3.) A reference sample from the same WS_2 growth and fabrication run was used to measure the optical strain response of unencapsulated devices, finding it consistent with previous literature (Supporting Information Figure S4).

Figure 2c shows the PL spectra of the same WS_2 device as Figure 2a before encapsulation, after AlO_x encapsulation but before imparting strain, and after biaxial strain. The A^0 exciton peak redshifts and becomes more symmetric (as indicated by the suppressed left shoulder peak) after AlO_x encapsulation and after imparting strain. The combined effect of encapsulation and strain causes a ~100 meV redshift of the A^0 exciton peak. Figure 2d shows how the A^0 exciton and shoulder peak positions evolve with strain. Consistent with our density functional theory simulations (shown in Supporting Information Section 8 and discussed later), the A^0 exciton peak redshifts by ~120 ± 61 meV/% strain. This is also in line with previous reports of WS_2 under biaxial tensile strain using a similar strain setup.[21]

https://doi.org/10.1021/acsnano.3c08996
ACS Nano 2024, 18, 18151−18159

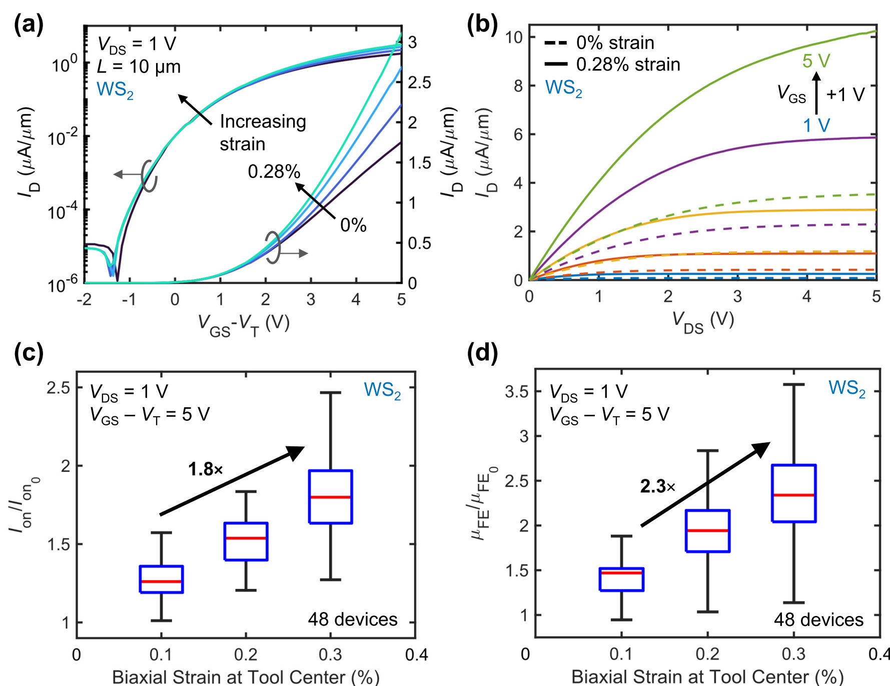

Figure 3. Strained WS_2 device measurements. (a) Transfer characteristics (I_D vs $V_{GS} - V_T$) of the device from Figure 1b (W = 20 μm, L = 10 μm) at different levels of applied biaxial tensile strain, where V_T is the constant-current threshold voltage. Same data are plotted both on a log scale (left y-axis) and a linear scale (right y-axis). (b) Output characteristics (I_D vs V_{DS}) of the same device at 0% (dashed) and 0.28% (solid) applied biaxial tensile strain for V_{GS} = 1 V (blue), 2 V (red), 3 V (yellow), 4 V (purple), and 5 V (green). Significant saturation current enhancement is seen with strain applied. (c) On-current (I_{on}) normalized to the initial unstrained values ($I_{on,0}$) for 48 transistors as a function of applied biaxial strain, with the box plots showing the median across devices (red lines), first and third quartiles (blue boxes), and maximum and minimum (top and bottom horizontal lines, respectively). (d) Field-effect mobility (μ_{FE}) normalized to the initial unstrained values for the same 48 transistors as in (c) as a function of applied strain. I_{on} and μ_{FE} values were extracted at V_{DS} = 1 V and $V_{GS} - V_T$ = 5 V.

We note that the AlO_x encapsulation alters the optical signatures of WS_2 (compared to unencapsulated samples), consistent with previous findings;[21,27,28] however, this does not affect our conclusions because all our strain measurements are relative to the strain tool itself. In other words, optical signatures of unencapsulated WS_2 are not used to calibrate the encapsulated samples. While a complete study of the combined effect of strain and dielectric encapsulation on Raman and PL shift rates is beyond the scope of this paper, there are at least four contributing factors: in-plane lattice deformation (from applied strain), cross-plane lattice deformation[29] (from the AlO_x encapsulation), doping from the encapsulation,[30] and remote phonon screening.[19] These may all affect the deformation potentials and the strength of electron−phonon coupling in the WS_2. For example, with biaxial tensile strain, the electron-A_1' phonon coupling strength may increase,[29] while the encapsulation layer may screen this effect due to interfacial charge transfer, resulting in no apparent shift in the A_1' phonon mode.

Electrical Measurements of WS_2 Devices under Strain. We next performed electrical measurements of our devices with applied biaxial strain. Our setup enables direct evaluation of our transistors under strain in a probe station, in ambient air (see Supporting Information Figure S2). We measured multiple devices on two separate flexible substrates to exclude possible degradation from multiple strain cycles. Figure 3a displays the drain current (I_D) vs gate voltage overdrive ($V_{GS} - V_T$) of the device from Figure 1b at V_{DS} = 1 V. Here, V_T is the threshold voltage estimated by the constant-current method[31] with a threshold current of I_D = 10 nA/μm, consistent with the International Roadmap for Devices and Systems (IRDS) 2022 threshold for high-performance devices.[32] (We compare the constant-current,[31] linear extrapolation,[31] and Y-function[33] methods of V_T extraction for our devices in Supporting Information Section 4.)

In Figure 3a, we plot I_D vs gate overdrive voltage to account for possible shifts in V_T and electron density due to strain, for several values of biaxial strain up to 0.28% (estimated based on its location relative to the center of the sample). Figure 3b shows the corresponding I_D vs V_{DS} measurements at 0% (dashed lines) and 0.28% (solid lines) biaxial tensile strain for V_{GS} from 1 to 5 V. The drain current increases with strain: for $V_{GS} = V_{DS}$ = 5 V, the drain current nearly triples from ~3.5 to ~10.2 μA/μm at 0.28% strain. We note that the output characteristics display current saturation with a nearly quadratic (in $V_{GS} - V_T$) dependence, emphasizing that this is a classic, "textbook-like" long-channel field-effect transistor. Additional information about the (small) hysteresis and gate leakage current for this device can be found in Supporting Information Section 5.

We estimate the on-state current (I_{on}) and field-effect mobility (μ_{FE}) from measurements (*e.g.* Figure 3a) in the linear region at the same gate overdrive ($V_{GS} - V_T$ = 5 V). In the linear regime, when $V_{DS} < V_{GS} - V_T$, the field-effect mobility is $\mu_{FE} = (\partial I_D/\partial V_{GS})L/(WC_{ox}V_{DS})$, where $C_{ox} \approx$ 378 nF/cm^2 is the gate capacitance per unit area. (The Al_2O_3 thickness was measured by ellipsometry on a reference silicon piece, and its dielectric constant was measured with metal−insulator−metal capacitors.[13]) The transistor shown in Figure 3a has $I_{on} \approx$ 1.8 μA/μm and $\mu_{FE} \approx$ 12 cm^2 V^{-1} s^{-1} without applied strain. At

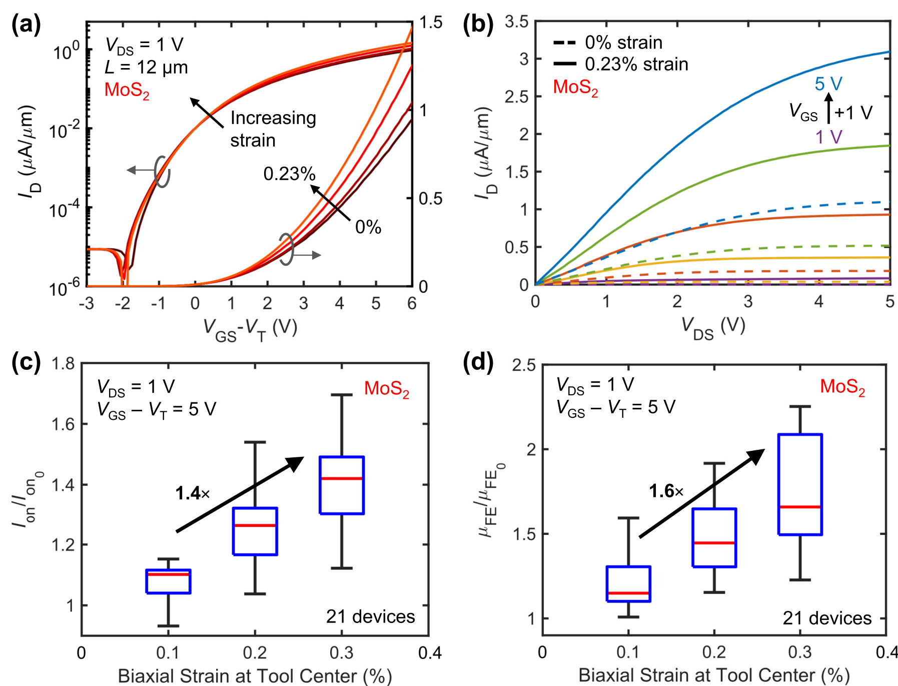

Figure 4. Strained MoS_2 device measurements. (a) Transfer characteristics (I_D vs $V_{GS} - V_T$) of a device with width W = 20 μm and channel length L = 12 μm at different levels of applied biaxial tensile strain, as in Figure 3a. (b) Output characteristics (I_D vs V_{DS}) of the same device at 0% (dashed) and 0.23% (solid) applied biaxial tensile strain for V_{GS} = 1 V (purple) to 5 V (blue). Significant saturation current enhancement is seen with strain applied, as in the WS_2 device. (c) On-current (I_{on}) normalized to the initial unstrained values ($I_{on,0}$) for 21 transistors as a function of applied biaxial strain, as in Figure 3c. (d) Field-effect mobility (μ_{FE}) normalized to the initial unstrained values ($\mu_{FE,0}$) for the same 21 transistors as in (c) as a function of applied strain. I_{on} and μ_{FE} values were extracted at V_{DS} = 1 V and $V_{GS} - V_T$ = 5 V.

0.3% applied biaxial tensile strain, the transistor has $I_{on} \approx 3.2$ μA/μm and $\mu_{FE} \approx 30.5$ cm^2 V^{-1} s^{-1}. Therefore, we achieve a 150% improvement in μ_{FE} at ~0.28% biaxial tensile strain for this device. [The current enhancement appears to be greater in saturation for the same device in Figure 3b, which does not adjust for V_T, because V_T decreases with strain. This effect is magnified by $\propto (V_{GS} - V_T)^2$ in saturation. See Supporting Information Figure S5 for changes in V_T with strain.]

We measure 47 other transistors with channel lengths from L = 2 to 15 μm on the same substrate and perform electrical measurements with applied strain. To account for device variation, we extract the I_{on} and μ_{FE} for all devices at all strain levels and report the improvements in I_{on} and μ_{FE} relative to their initial values without applied strain, as summarized in Figure 3c,d. On average, for WS_2, I_{on} increases by a factor of 1.8 ± 0.4, and μ_{FE} increases by a factor of 2.3 ± 0.5 at 0.3% applied tensile strain at tool center, compared to the initial values without strain. If V_T is estimated with the linear extrapolation and Y-function methods, the improvement factor is higher for both I_{on} and μ_{FE} (see Supporting Information Figure S5). Our μ_{FE} improvements due to biaxial tensile strain of WS_2 exceed previous improvements seen in uniaxial tensile strain studies on MoS_2 field-effect transistors.[13]

In Figure 3, we reported device behavior up to 0.3% applied biaxial tensile strain. The devices recover to their initial states after the strain is removed (Supporting Information Figure S10.) However, for 0.4% biaxial strain at the tool center, over half of the devices showed a degradation in I_{on} and μ_{FE} or did not generate enough current for constant-current V_T extraction, likely due to strain-induced defects in the gate dielectric or poorer adhesion at the contact-WS_2 interface. (See Supporting Information Section 6 for device relaxation and degradation after higher strain.) Due to the nonuniform strain field imparted by the tool geometry,[23] we examine the impact of device location on I_{on} and μ_{FE} improvement. Supporting Information Section 7 shows heat maps for the strain evolution of I_{on} and μ_{FE} for each measured device. There was no significant difference between the devices that experienced more longitudinal (i.e., along-channel) strain compared to the devices that experienced more transverse (i.e., across-channel) strain. We attribute this to the isotropic in-plane conduction band valleys in WS_2[22] and random orientation of grain boundaries in the channels. Therefore, tensile strain in any direction may have an additive effect of increased I_{on} and μ_{FE}, producing larger I_{on} and μ_{FE} improvements for biaxial tensile strain compared to those for uniaxial tensile strain.

Electrical Measurements of MoS_2 Devices under Biaxial Strain. We repeat the strained electrical measurements for one flexible chiplet of monolayer MoS_2 transistors with the same device structure and fabrication process, but without the AlO_x capping layer, which can introduce excessive doping and hysteresis in MoS_2 unless annealed at temperatures beyond the thermal budget of the PEN.[30] Figure 4a,b displays the I_D vs $V_{GS} - V_T$ and the corresponding I_D vs V_{DS} curves, respectively, for a device with channel width W = 20 μm and channel length L = 12 μm as a function of strain, up to 0.23% strain. This device showed an increase in I_{on} from ~0.75 to ~1.13 μA/μm and an increase in μ_{FE} from ~5.4 to ~9.1 cm^2 V^{-1} s^{-1} at ~0.23% strain, equating to a 50% increase in I_{on} and 70% increase in μ_{FE} at V_{DS} = 1 V and overdrive $V_{GS} - V_T$ = 5 V. Similar to WS_2, the saturation current for this MoS_2 device nearly triples from 1.1 to 3.1 μA/μm with 0.23% biaxial tensile strain at $V_{GS} = V_{DS}$ = 5 V.

https://doi.org/10.1021/acsnano.3c08996
ACS Nano 2024, 18, 18151−18159

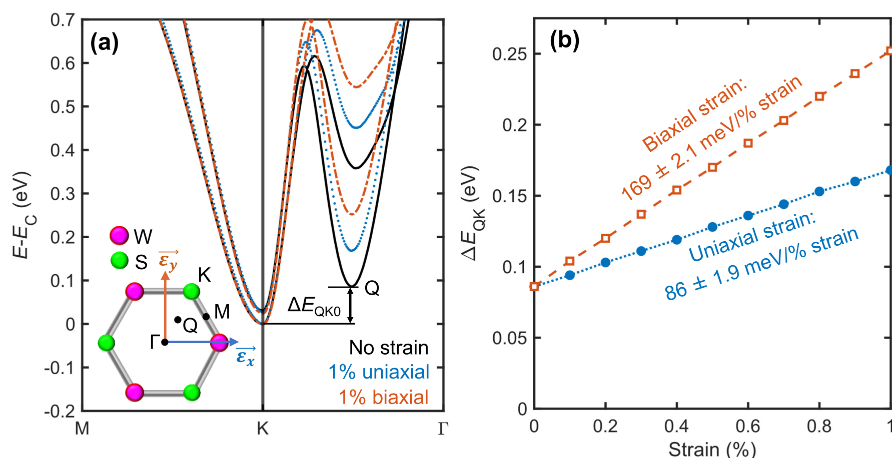

Figure 5. Density functional theory (DFT) calculations. (a) Conduction band of monolayer WS_2 without strain (black lines), 1% uniaxial strain (blue dotted lines), and 1% biaxial strain (orange dashed lines) relative to the lowest (K-valley) band edge (E_C). Two conduction bands are seen for each case, due to spin splitting. Inset shows the unit cell and applied strain vectors $\vec{\varepsilon_x}$ and $\vec{\varepsilon_y}$ used in the simulation. (b) Energy separation between K and Q conduction band valleys (ΔE_{QK}) as a function of applied tensile strain. ΔE_{QK} increases with strain and at a higher rate for biaxial than for uniaxial tensile strain, and such valley splitting causes a reduction of K−Q intervalley scattering. The calculated ΔE_{QK0} without strain (~87 meV) accounting for spin−orbit coupling is consistent with that of Gaddemane et al.[34]

We measure 20 other transistors with channel lengths from $L = 2$ to 15 μm on the same substrate, extracting and reporting the I_{on} and μ_{FE} in a similar manner as for the WS_2 sample. On average, for MoS_2, I_{on} increases by a factor of 1.4 ± 0.26, and μ_{FE} increases similarly by a factor of 1.6 ± 0.16 at 0.3% applied biaxial tensile strain at the tool center, compared to the initial values without strain. These values are slightly lower than those of WS_2 because the measured devices were on average 5% farther away from the center of the sample than those of the WS_2 sample. (See Supporting Information Section 7 for a discussion of the strain fields induced by the tool.)

Simulations and Discussion. To understand the causes of mobility enhancement in our biaxially strained devices, we turn to density functional theory (DFT) simulations with spin−orbit coupling, which plays a stronger role in W-based materials.[34] From previous work on TMDs and other semiconductors (including Si), one can expect that strain affects the energy band gap, the electron effective masses, and intervalley electron−phonon scattering rates.[13,14,16,19,35,36]

From our experiments (Figure 2d) and simulations (Supporting Information Figure S12), biaxial strain reduces the WS_2 band gap and consequently the transistor threshold voltage V_T (Supporting Information Figure S5). However, the V_T shift due to strain is small (<0.5 V for our devices, depending on extraction method) compared to the gate voltage overdrive used (5 V). We also report I_{on} and μ_{FE} at a constant gate overdrive to account for the V_T shift due to strain, ruling out band gap reduction as a primary contributor to strain-related mobility improvements in our devices. Regarding changes of effective mass, both our DFT simulations (Figure 5a) and previous work[16] suggest that for the range of biaxial strains applied in our experiments, the curvature of the conduction band at the K point changes only minimally and cannot be responsible for the observed mobility enhancement.

Our DFT simulations show a much greater effect of biaxial strain on the K−Q valley separation (ΔE_{QK}), which is known to control electron−phonon intervalley scattering and therefore mobility.[36] (The Q point is on the T line approximately halfway between the K and the Γ points.[37]) Figure 5b plots the evolution of ΔE_{QK} with both uniaxial and biaxial tensile strain, showing a nearly linear increase within the range considered here. Uniaxial tensile strain increases ΔE_{QK} by 86 ± 1.9 meV/% strain, and biaxial tensile strain increases ΔE_{QK} by almost twice as much, 169 ± 2.1 meV/% strain. The greater change in ΔE_{QK} with biaxial tensile strain suggests a higher mobility improvement for WS_2 under these conditions. At the 0.3% strain applied in our experiments, ΔE_{QK} increases by ~40 meV. While this is less than $2k_BT$ at room temperature, theoretical studies[16,38] have predicted that even small changes in ΔE_{QK} can lead to large changes in mobility by altering the occupational probability of electrons in the upper conduction band Q-valley and modulating the electron−phonon coupling strength, which controls intervalley scattering.

We compare our experimental observations between WS_2 and MoS_2 and with the DFT calculations. For example, we note that WS_2 is expected to have larger spin−orbit coupling and smaller unstrained ΔE_{QK0} than MoS_2,[34] which may cause different strain-dependent scattering rates in the two materials. However, experimentally, we find that biaxial tensile strain leads to similar improvement in I_{on} and μ_{FE} for both WS_2 and MoS_2. This is consistent with previous calculations that do not predict a substantial difference in the effect of strain on transport characteristics between the two materials.[16] In addition, for the time being, any differences in measured mobility can be attributed to experimental (i.e., fabrication-related) variation between devices[6] and some nonuniformity in the applied strain (see Supporting Information Section 7).

Finally, we comment on the possible role of tensile strain on defects and contacts. Defect trap states in the TMD or at the TMD−gate dielectric interface may facilitate hopping-like electron transport. Applied tensile strain can modulate the energy locations of these trap states in relation to the conduction band edge, increasing carrier lifetimes[39] and improving channel conduction. This process is not well-understood, and future work should explore the fundamental role of strain on defects in TMDs. Tensile strain may also lower Schottky barriers[40] at TMD transistor contacts, reducing the contact resistance.[41,42] While these effects have been shown in MoS_2, our TMD device dimensions are large (~10 μm), reducing the influence of the contacts. We do not see a

https://doi.org/10.1021/acsnano.3c08996
ACS Nano 2024, 18, 18151−18159

dependence of the strain enhancement effects on channel length (between 2 and 15 μm, as shown in Supporting Information Figure S13), and our transistors display classic long-channel behavior (Figure 3b), suggesting that contacts do not play a dominant role in our measurements.

CONCLUSIONS

We report the on-state current and mobility enhancement of CVD-grown monolayer WS_2 and MoS_2 transistors with applied biaxial tensile strain. Devices were strained on flexible PEN substrates through the deflection of an acrylic cross with a motorized precision lead screw. On average, at 0.3% biaxial tensile strain, the WS_2 devices experienced a ∼2× increase of electron mobility and on-state drain current; this is the largest mobility improvement of TMD transistors with the lowest applied tensile strain to date, vs previous experimental work demonstrating the same increase at higher (0.7%) uniaxial tensile strain for MoS_2.[13] Based on DFT simulations, we attribute this improvement to reduced intervalley scattering from the increased energy separation ΔE_{QK} under tensile strain. (The theoretical upper bounds of mobility enhancement with biaxial tensile strain in WS_2 could be >10× when only intrinsic phonons are included and >3× when remote phonons and charge impurities are also accounted for.[16]) Our results highlight strain engineering as a key future performance enhancer for TMD devices in both flexible and traditional rigid electronics and optoelectronics.

METHODS

Device Fabrication and Layer Transfer. We fabricated locally back-gated monolayer TMD field-effect transistors on flexible, transparent poly(ethylene naphthalate) (PEN, Dupont Teijin Films, 125 μm thick) sheets. Monolayer WS_2 was grown[43] by chemical vapor deposition (CVD) onto *c*-plane sapphire substrates dip-coated in aqueous ammonium metatungstate (AMT) precursor (see Supporting Information Section 1). Monolayer MoS_2 was grown by solid-source CVD onto 90 nm SiO_2/Si substrates.[6] Separately, PEN substrates were prepared with Al_2O_3 dielectrics on prepatterned metal back-gates (Figure 1a). After growth, the TMDs were then transferred with a PMMA/polystyrene bilayer stamp to the PEN with patterned local back-gates and Al_2O_3 gate oxide. The 5 nm/45 nm Ni/Au contacts are patterned by optical lithography and lift-off, and additional steps are provided in Supporting Information Section 1. To improve the device performance, we encapsulated the devices with substoichiometric AlO_x deposited by first electron-beam evaporating a ∼1.5 nm Al seed layer followed by ∼8.5 nm Al_2O_3 via thermal atomic layer deposition at 130 °C. The substoichiometric AlO_x encapsulation anneals the sample and imparts some strain into the WS_2 due to thermal expansion effects.[30,44] Due to the low glass transition temperature of PEN, we limited the thermal budget to ensure no degradation in the substrate due to processing. Once device fabrication was complete, the sample was attached to the 3 mm thick acrylic cruciform via commercially available cyanoacrylate adhesive and allowed to cure in air at room temperature for 48 h.

Raman and Photoluminescence Spectroscopy. We took Raman and photoluminescence measurements using a Horiba Labram HR Evolution Raman System at the Stanford Nanofabrication Shared Facility. We used a green 532 nm laser with 1% incident laser power (0.5 mW) to avoid heating. The laser spot size was less than 1 μm, and for maps, we used a spacing of at least 1.6 μm between each point to ensure that each measured spot on the sample was distinct. Peak fitting details can be found in Supporting Information Section 3.

Electrical Measurements. We used an air probe station with a Keithley 4200 semiconductor parameter analyzer to conduct our electrical measurements. All electrical measurements under strain were taken with the PEN sample attached to the acrylic cross to ensure that the sample attachment process did not impact the measurements. The measurements were performed in the dark at room temperature. Prior to measurement, some regions of the AlO_x encapsulation layer were patterned and wet etched with Megaposit MF-26A developer for 10 min to access the contact pads. Forward and backward voltage sweeps were taken for every measurement; a discussion of hysteresis can be found in Supporting Information, Section 5.

Density Functional Theory Calculations. Density functional theory (DFT) calculations were performed using Quantum ESPRESSO[45] version 7.1. We use fully relativistic norm-conserving Vanderbilt pseudopotentials[46,47] and include the effect of spin−orbit coupling, which has been shown to significantly affect the band structure of WS_2.[34] All calculations were performed on $31 \times 31 \times 1$ *k*-point grids with kinetic energy cutoffs of 70 Ry and charge density and potential cutoffs of 560 Ry. Additional details can be found in Supporting Information Section 8.

ASSOCIATED CONTENT

Supporting Information

The Supporting Information is available free of charge at https://pubs.acs.org/doi/10.1021/acsnano.3c08996.

> Device fabrication process, effect of encapsulation on WS_2 devices, Raman and photoluminescence spectroscopy measurement parameters and peak fitting, threshold voltage estimates, current−voltage characteristics of devices under strain, WS_2 devices at higher strain and after strain relaxation, strain fields induced by the biaxial strain tool, density functional theory calculations of full WS_2 band structure, and channel length dependence of strain-induced mobility improvements (PDF)

AUTHOR INFORMATION

Corresponding Author

Eric Pop − *Department of Electrical Engineering, Stanford University, Stanford, California 94305, United States; Department of Materials Science & Engineering and Precourt Institute for Energy, Stanford University, Stanford, California 94305, United States;* orcid.org/0000-0003-0436-8534; Email: epop@stanford.edu

Authors

Jerry A. Yang − *Department of Electrical Engineering, Stanford University, Stanford, California 94305, United States;* orcid.org/0000-0001-5521-8523

Robert K. A. Bennett − *Department of Electrical Engineering, Stanford University, Stanford, California 94305, United States;* orcid.org/0000-0001-7427-8724

Lauren Hoang − *Department of Electrical Engineering, Stanford University, Stanford, California 94305, United States;* orcid.org/0009-0001-7556-8560

Zhepeng Zhang − *Department of Materials Science & Engineering, Stanford University, Stanford, California 94305, United States;* orcid.org/0000-0002-9870-0720

Kamila J. Thompson − *Department of Electrical Engineering, Stanford University, Stanford, California 94305, United States*

Antonios Michail − *Department of Physics, University of Patras, Patras 26504, Greece; Foundation for Research and Technology Hellas, Institute of Chemical Engineering Sciences (FORTH - ICE/HT), Patras 26504, Greece;* orcid.org/0000-0002-8428-6602

John Parthenios − *Foundation for Research and Technology Hellas, Institute of Chemical Engineering Sciences (FORTH -*

https://doi.org/10.1021/acsnano.3c08996
ACS Nano 2024, 18, 18151−18159

ICE/HT), Patras 26504, Greece; orcid.org/0000-0001-6066-7120

Konstantinos Papagelis − *Foundation for Research and Technology Hellas, Institute of Chemical Engineering Sciences (FORTH - ICE/HT), Patras 26504, Greece; School of Physics, Department of Solid State Physics, Aristotle University of Thessaloniki, Thessaloniki 54124, Greece;* orcid.org/0000-0001-5094-9837

Andrew J. Mannix − *Department of Materials Science & Engineering, Stanford University, Stanford, California 94305, United States; Stanford Institute for Materials and Energy Sciences, SLAC National Accelerator Laboratory, Menlo Park, California 94305, United States;* orcid.org/0000-0003-4788-1506

Complete contact information is available at:
https://pubs.acs.org/10.1021/acsnano.3c08996

Author Contributions

The manuscript was written through contributions of all authors. All authors have given approval to the final version of the manuscript.

Notes

The authors declare no competing financial interest.

Land Acknowledgement. This work was completed at Stanford University, on the ancestral land of the Muwekma Ohlone Tribe, which continues to be of great importance to the Ohlone people. We acknowledge and honor our institution's relationship to Indigenous peoples and their continual care for the land we use to conduct scientific research.[48]

Preprint Statement. This work was first submitted to arXiv on September 19, 2023. The preprint version can be found at: Yang, J. A.; Bennett, R. K. A.; Hoang, L.; Zhang, Z.; Thompson, K. J.; Michail, A.; Parthenios, J.; Papagelis, K.; Mannix, A. J.; Pop, E. Biaxial Tensile Strain Enhances Electron Mobility of Monolayer Transition Metal Dichalcogenides. 2023, arXiv:2309.10939. arXiv. https://arxiv.org/abs/2309.10939 (accessed Feb. 7, 2024).

ACKNOWLEDGMENTS

This work was completed in part at the Stanford Nanofabrication and Stanford Nano Shared Facilities, which receive funding from the National Science Foundation (NSF) as part of the National Nanotechnology Coordinated Infrastructure (NNCI) Award ECCS-1542152. The work was also supported in part by the Stanford SystemX Alliance and by Intel Corporation. J.A.Y. acknowledges support from the NSF Graduate Research Fellowship. R.K.A.B acknowledges support from the Stanford Graduate Fellowship and NSERC PGS-D program. Z.Z. and A.J.M. acknowledge support from the US Department of Energy for the development of WS_2 synthesis, under award DE-SC0021984. K.J.T. acknowledges support from the Stanford Summer Undergraduate Research Program. We thank Isha Datye, Marc Jaikissoon, Crystal Nattoo, Alwin Daus, and Ajay Sood for their valuable discussions. We would also like to thank Jihun Rho for being an excellent hand model for Figure 1c.

REFERENCES

(1) Das, S.; Sebastian, A.; Pop, E.; McClellan, C. J.; Franklin, A. D.; Grasser, T.; Knobloch, T.; Illarionov, Y.; Penumatcha, A. V.; Appenzeller, J.; Chen, Z.; Zhu, W.; Asselberghs, I.; Li, L.-J.; Avci, U. E.; Bhat, N.; Anthopoulos, T. D.; Singh, R. Transistors Based on Two-Dimensional Materials for Future Integrated Circuits. *Nat. Electron.* **2021**, *4* (11), 786−799.

(2) Liu, Y.; Weiss, N. O.; Duan, X.; Cheng, H.-C.; Huang, Y.; Duan, X. Van Der Waals Heterostructures and Devices. *Nat. Rev. Mater.* **2016**, *1* (9), 1−17.

(3) Pal, A.; Agashiwala, K.; Jiang, J.; Zhang, D.; Chavan, T.; Kumar, A.; Yeh, C.-H.; Cao, W.; Banerjee, K. Two-Dimensional Materials Enabled Next-Generation Low-Energy Compute and Connectivity. *MRS Bull.* **2021**, *46* (12), 1211−1228.

(4) Chubarov, M.; Choudhury, T. H.; Hickey, D. R.; Bachu, S.; Zhang, T.; Sebastian, A.; Bansal, A.; Zhu, H.; Trainor, N.; Das, S.; Terrones, M.; Alem, N.; Redwing, J. M. Wafer-Scale Epitaxial Growth of Unidirectional WS_2 Monolayers on Sapphire. *ACS Nano* **2021**, *15* (2), 2532−2541.

(5) Lan, F.; Yang, R.; Sun, K.; Wang, Z.; Zhang, Y.; Wang, Y.; Cheng, H. Growth of Wafer Scale Continuous Monolayer WS_2 Film with Millimeter Grain Size. *Vacuum* **2022**, *201*, 111091.

(6) Smithe, K. K. H.; Suryavanshi, S. V.; Muñoz Rojo, M.; Tedjarati, A. D.; Pop, E. Low Variability in Synthetic Monolayer MoS_2 Devices. *ACS Nano* **2017**, *11* (8), 8456−8463.

(7) English, C. D.; Shine, G.; Dorgan, V. E.; Saraswat, K. C.; Pop, E. Improved Contacts to MoS_2 Transistors by Ultra-High Vacuum Metal Deposition. *Nano Lett.* **2016**, *16* (6), 3824−3830.

(8) Das, S.; Appenzeller, J. WSe_2 Field Effect Transistors with Enhanced Ambipolar Characteristics. *Appl. Phys. Lett.* **2013**, *103* (10), 103501.

(9) Lee, G.; Oh, S.; Kim, J.; Kim, J. Ambipolar Charge Transport in Two-Dimensional WS_2 Metal-Insulator-Semiconductor and Metal-Insulator-Semiconductor Field-Effect Transistors. *ACS Appl. Mater. Interfaces* **2020**, *12* (20), 23127−23133.

(10) Kumar, A.; Nazif, K. N.; Ramesh, P.; Saraswat, K. Doped WS_2 Transistors with Large on-off Ratio and High on-Current. *2020 Device Research Conference (DRC)* **2020**, 1.

(11) Dorow, C.; O'Brien, K.; Naylor, C. H.; Lee, S.; Penumatcha, A.; Hsiao, A.; Tronic, T.; Christenson, M.; Maxey, K.; Zhu, H.; Oni, A.; Alaan, U.; Gosavi, T.; Gupta, A. S.; Bristol, R.; Clendenning, S.; Metz, M.; Avci, U. Advancing Monolayer 2-D nMOS and pMOS Transistor Integration From Growth to Van Der Waals Interface Engineering for Ultimate CMOS Scaling. *IEEE Trans. Electron Devices* **2021**, *68* (12), 6592−6598.

(12) O'Brien, K. P.; Dorow, C. J.; Penumatcha, A.; Maxey, K.; Lee, S.; Naylor, C. H.; Hsiao, A.; Holybee, B.; Rogan, C.; Adams, D.; Tronic, T.; Ma, S.; Oni, A.; Gupta, A. S.; Bristol, R.; Clendenning, S.; Metz, M.; Avci, U. Advancing 2D Monolayer CMOS Through Contact, Channel and Interface Engineering. *2021 IEEE International Electron Devices Meeting (IEDM)* **2021**, 7.1.1−7.1.4.

(13) Datye, I. M.; Daus, A.; Grady, R. W.; Brenner, K.; Vaziri, S.; Pop, E. Strain-Enhanced Mobility of Monolayer MoS_2. *Nano Lett.* **2022**, *22* (20), 8052−8059.

(14) Yun, W. S.; Han, S. W.; Hong, S. C.; Kim, I. G.; Lee, J. D. Thickness and Strain Effects on Electronic Structures of Transition Metal Dichalcogenides: 2H-MX_2 Semiconductors (M = Mo, W; X = S, Se, Te). *Phys. Rev. B* **2012**, *85* (3), 033305.

(15) Amin, B.; Kaloni, T. P.; Schwingenschlögl, U. Strain Engineering of WS_2, WSe_2, and WTe_2. *RSC Adv.* **2014**, *4* (65), 34561−34565.

(16) Hosseini, M.; Elahi, M.; Pourfath, M.; Esseni, D. Strain-Induced Modulation of Electron Mobili ty in Single-Layer Transition Metal Dichalcogenides MX_2 (M = Mo, W; X = S, Se). *IEEE Trans. Electron Devices* **2015**, *62* (10), 3192−3198.

(17) Cheng, L.; Zhang, C.; Liu, Y. Intrinsic Charge Carrier Mobility of 2D Semiconductors. *Comput. Mater. Sci.* **2021**, *194*, 110468.

(18) Zhang, C.; Cheng, L.; Liu, Y. Understanding High-Field Electron Transport Properties and Strain Effects of Monolayer Transition Metal Dichalcogenides. *Phys. Rev. B* **2020**, *102* (11), 115405.

(19) Hosseini, M.; Elahi, M.; Pourfath, M.; Esseni, D. Strain Induced Mobility Modulation in Single-Layer MoS_2. *J. Phys. Appl. Phys.* **2015**, *48* (37), 375104.

(20) Mistry, K.; Armstrong, M.; Auth, C.; Cea, S.; Coan, T.; Ghani, T.; Hoffmann, T.; Murthy, A.; Sandford, J.; Shaheed, R.; Zawadzki, K.; Zhang, K.; Thompson, S.; Bohr, M. Delaying Forever: Uniaxial Strained Silicon Transistors in a 90nm CMOS Technology. *Digest of Technical Papers. 2004 Symposium on VLSI Technology, 2004.* **2004**, 50–51.

(21) Michail, A.; Anestopoulos, D.; Delikoukos, N.; Grammatikopoulos, S.; Tsirkas, S. A.; Lathiotakis, N. N.; Frank, O.; Filintoglou, K.; Parthenios, J.; Papagelis, K. Tuning the Photoluminescence and Raman Response of Single-Layer WS_2 Crystals Using Biaxial Strain. *J. Phys. Chem. C* **2023**, *127* (7), 3506–3515.

(22) Jin, Z.; Li, X.; Mullen, J. T.; Kim, K. W. Intrinsic Transport Properties of Electrons and Holes in Monolayer Transition-Metal Dichalcogenides. *Phys. Rev. B* **2014**, *90* (4), 045422.

(23) Michail, A.; Anestopoulos, D.; Delikoukos, N.; Parthenios, J.; Grammatikopoulos, S.; Tsirkas, S. A.; Lathiotakis, N. N.; Frank, O.; Filintoglou, K.; Papagelis, K. Biaxial Strain Engineering of CVD and Exfoliated Single- and Bi-Layer MoS_2 Crystals. *2D Mater.* **2021**, *8* (1), 015023.

(24) Michail, A.; Yang, J. A.; Filintoglou, K.; Balakeras, N.; Nattoo, C.; Bailey, C. S.; Daus, A.; Parthenios, J.; Pop, E.; Papagelis, K. Biaxial Strain Transfer in Monolayer MoS_2 and WSe_2 Transistor Structures. Submitted for publication (**2024**).

(25) Wan, Y.; Li, E.; Yu, Z.; Huang, J.-K.; Li, M.-Y.; Chou, A.-S.; Lee, Y.-T.; Lee, C.-J.; Hsu, H.-C.; Zhan, Q.; Aljarb, A.; Fu, J.-H.; Chiu, S.-P.; Wang, X.; Lin, J.-J.; Chiu, Y.-P.; Chang, W.-H.; Wang, H.; Shi, Y.; Lin, N.; Cheng, Y.; Tung, V.; Li, L.-J. Low-Defect-Density WS_2 by Hydroxide Vapor Phase Deposition. *Nat. Commun.* **2022**, *13* (1), 4149.

(26) Liang, Q.; Gou, J.; Arramel; Zhang, Q.; Zhang, W.; Wee, A. T. S. Oxygen-Induced Controllable p-Type Doping in 2D Semiconductor Transition Metal Dichalcogenides. *Nano Res.* **2020**, *13* (12), 3439–3444.

(27) Zhang, Q.; Chang, Z.; Xu, G.; Wang, Z.; Zhang, Y.; Xu, Z.-Q.; Chen, S.; Bao, Q.; Liu, J. Z.; Mai, Y.-W.; Duan, W.; Fuhrer, M. S.; Zheng, C. Strain Relaxation of Monolayer WS_2 on Plastic Substrate. *Adv. Funct. Mater.* **2016**, *26* (47), 8707–8714.

(28) Li, Z.; Lv, Y.; Ren, L.; Li, J.; Kong, L.; Zeng, Y.; Tao, Q.; Wu, R.; Ma, H.; Zhao, B.; Wang, D.; Dang, W.; Chen, K.; Liao, L.; Duan, X.; Duan, X.; Liu, Y. Efficient Strain Modulation of 2D Materials via Polymer Encapsulation. *Nat. Commun.* **2020**, *11* (1), 1151.

(29) Sohier, T.; Ponomarev, E.; Gibertini, M.; Berger, H.; Marzari, N.; Ubrig, N.; Morpurgo, A. F. Enhanced Electron-Phonon Interaction in Multivalley Materials. *Phys. Rev. X* **2019**, *9* (3), 031019.

(30) McClellan, C. J.; Yalon, E.; Smithe, K. K. H.; Suryavanshi, S. V.; Pop, E. High Current Density in Monolayer MoS_2 Doped by AlO_x. *ACS Nano* **2021**, *15* (1), 1587–1596.

(31) Ortiz-Conde, A.; García-Sánchez, F. J.; Muci, J.; Terán Barrios, A.; Liou, J. J.; Ho, C.-S. Revisiting MOSFET Threshold Voltage Extraction Methods. *Microelectron. Reliab.* **2013**, *53* (1), 90–104.

(32) *International Roadmap for Devices and Systems 2022*; Institute of Electrical and Electronics Engineers, 2022. https://irds.ieee.org/editions/2022 (accessed 2023–07–07).

(33) Pacheco-Sanchez, A.; Jiménez, D. Accuracy of Y -Function Methods for Parameters Extraction of Two-Dimensional FETs across Different Technologies. *Electron. Lett.* **2020**, *56* (18), 942–945.

(34) Gaddemane, G.; Gopalan, S.; Van de Put, M. L.; Fischetti, M. V. Limitations of Ab Initio Methods to Predict the Electronic-Transport Properties of Two-Dimensional Semiconductors: The Computational Example of 2H-Phase Transition Metal Dichalcogenides. *J. Comput. Electron.* **2021**, *20* (1), 49–59.

(35) Chang, C.-H.; Fan, X.; Lin, S.-H.; Kuo, J.-L. Orbital Analysis of Electronic Structure and Phonon Dispersion in MoS_2, $MoSe_2$, WS_2, and WSe_2 Monolayers under Strain. *Phys. Rev. B* **2013**, *88* (19), 195420.

(36) Ferry, D. K. Electron Transport in Some Transition Metal Di-Chalcogenides: MoS_2 and WS_2. *Semicond. Sci. Technol.* **2017**, *32* (8), 085003.

(37) Ribeiro-Soares, J.; Almeida, R. M.; Barros, E. B.; Araujo, P. T.; Dresselhaus, M. S.; Cançado, L. G.; Jorio, A. Group Theory Analysis of Phonons in Two-Dimensional Transition Metal Dichalcogenides. *Phys. Rev. B* **2014**, *90* (11), 115438.

(38) Sohier, T.; de Melo, P. M. M. C.; Zanolli, Z.; Verstraete, M. J. The Impact of Valley Profile on the Mobility and Kerr Rotation of Transition Metal Dichalcogenides. *2D Mater.* **2023**, *10* (2), 025006.

(39) Hong, H.; Cheng, Y.; Wu, C.; Huang, C.; Liu, C.; Yu, W.; Zhou, X.; Ma, C.; Wang, J.; Zhang, Z.; Zhao, Y.; Xiong, J.; Liu, K. Modulation of Carrier Lifetime in MoS_2 Monolayer by Uniaxial Strain. *Chin. Phys. B* **2020**, *29* (7), 077201.

(40) John, A. P.; Thenapparambil, A.; Thalakulam, M. Strain-Engineering the Schottky Barrier and Electrical Transport on MoS_2. *Nanotechnology* **2020**, *31* (27), 275703.

(41) Shen, T.; Penumatcha, A. V.; Appenzeller, J. Strain Engineering for Transition Metal Dichalcogenides Based Field Effect Transistors. *ACS Nano* **2016**, *10* (4), 4712–4718.

(42) Jaikissoon, M.; Köroglu, Ç.; Yang, J. A.; Neilson, K. M.; Saraswat, K. C.; Pop, E. CMOS-compatible Strain Engineering for High-Performance Monolayer Semiconductor Transistors. *arXiv*, 2022, preprint 2405.09792. https://arxiv.org/abs/2405.09792.

(43) Zhang, Z.; Hoang, L.; Hocking, M.; Hu, J.; Zaborski, G., Jr.; Reddy, P.; Dollard, J.; Goldhaber-Gordon, D.; Heinz, T. F.; Pop, E.; Mannix, A. J. Chemically Tailored Growth of 2D Semiconductors via Hybrid Metal-Organic Chemical Vapor Deposition. *arXiv* 2024, preprint 2403.03482. https://arxiv.org/abs/2403.03482.

(44) Ylivaara, O. M. E.; Liu, X.; Kilpi, L.; Lyytinen, J.; Schneider, D.; Laitinen, M.; Julin, J.; Ali, S.; Sintonen, S.; Berdova, M.; Haimi, E.; Sajavaara, T.; Ronkainen, H.; Lipsanen, H.; Koskinen, J.; Hannula, S.-P.; Puurunen, R. L. Aluminum Oxide from Trimethylaluminum and Water by Atomic Layer Deposition: The Temperature Dependence of Residual Stress, Elastic Modulus, Hardness and Adhesion. *Thin Solid Films* **2014**, *552*, 124–135.

(45) Giannozzi, P.; Baseggio, O.; Bonfà, P.; Brunato, D.; Car, R.; Carnimeo, I.; Cavazzoni, C.; de Gironcoli, S.; Delugas, P.; Ferrari Ruffino, F.; Ferretti, A.; Marzari, N.; Timrov, I.; Urru, A.; Baroni, S. Quantum ESPRESSO toward the Exascale. *J. Chem. Phys.* **2020**, *152* (15), 154105.

(46) Schlipf, M.; Gygi, F. Optimization Algorithm for the Generation of ONCV Pseudopotentials. *Comput. Phys. Commun.* **2015**, *196*, 36–44.

(47) Scherpelz, P.; Govoni, M.; Hamada, I.; Galli, G. Implementation and Validation of Fully Relativistic GW Calculations: Spin-Orbit Coupling in Molecules, Nanocrystals, and Solids. *J. Chem. Theory Comput.* **2016**, *12* (8), 3523–3544.

(48) *Stanford's Relationships with Native Peoples*; Stanford University. https://www.stanford.edu/native-peoples-relationship/ (accessed 2023-09-18).

https://doi.org/10.1021/acsnano.3c08996
ACS Nano 2024, 18, 18151–18159

Supporting Information

Biaxial Tensile Strain Enhances Electron Mobility of Monolayer Transition Metal Dichalcogenides

Jerry A. Yang[1], Robert K. A. Bennett[1], Lauren Hoang[1], Zhepeng Zhang[2], Kamila J. Thompson[1], Antonios Michail[3,4], John Parthenios[4], Konstantinos Papagelis[4,5], Andrew J. Mannix[2,6], Eric Pop[1,2,7,*]

[1]*Department of Electrical Engineering, Stanford University, Stanford, CA 94305, USA*
[2]*Department of Materials Science & Engineering, Stanford University, Stanford, CA 94305, USA*
[3]*Department of Physics, University of Patras, Patras, 26504, Greece*
[4]*Foundation for Research and Technology Hellas, Institute of Chemical Engineering Sciences (FORTH - ICE/HT), Patras, 26504, Greece*
[5]*School of Physics, Department of Solid State Physics, Aristotle University of Thessaloniki, Thessaloniki, 54124, Greece*
[6]*Stanford Institute for Materials and Energy Sciences, SLAC National Accelerator Laboratory, Menlo Park, CA 94305, USA*
[7]*Precourt Institute for Energy, Stanford University, Stanford, CA 94305, USA*

*Corresponding Author: epop@stanford.edu

1. TMD device fabrication process

Figure S1 describes and illustrates the WS_2 transistor fabrication process on polyethylene naphthalate (PEN) substrates of 2×2 cm^2. We first pattern the back-gate onto 125-µm thick polyethylene naphthalate (PEN) substrates with optical lithography, depositing Ti/Au (5 nm/40 nm) using electron-beam (e-beam) evaporation, and defining the back-gate by lift-off. We then deposit ~16 nm alumina (Al_2O_3) gate dielectric with atomic layer deposition (ALD) in a Savannah S200 from Cambridge Nanotech using trimethyl aluminum (TMA) and DI water as precursors for 200 cycles. The ALD was completed at 130 °C for ~3 hours to remain within the thermal budget of PEN.

We grow monolayer WS_2 on 50 mm diameter *c*-plane sapphire wafers, cleaved into quarters, by chemical vapor deposition (CVD) at 775 °C for 6 hours using diethyl sulfide (DES) and ammonium metatungstate (AMT) precursors, with potassium hydroxide growth promoter and Ar/H_2 carrier gases. Flow rates during growth are 0.05 sccm DES, 1600 sccm Ar, and 1 sccm H_2. The full details of this growth process will be discussed in a forthcoming paper. In addition, we grow monolayer MoS_2 by CVD on 2×2 cm^2 chips of 90 nm thermal SiO_2/Si wafers, using solid MoO_3 and S precursors.[1] The wafers are treated with an hexamethyldisilazane (HMDS) vapor prime, and drops of perylene-3,4,9,10-tetracarboxylic acid tetrapotassium acid salt (PTAS) are placed around the edges of the chips as a growth promoter. The samples are placed in a 50 mm diameter tube furnace with the precursors, and the growth is completed at 750 °C for 5 min at 800 Torr. 30 sccm Ar is used as the carrier gas.

After growth, we transfer the materials (either WS_2 or MoS_2) onto the samples with an approach similar to Vaziri *et al*.[2] We next define the rectangular channel using an O_2 plasma etch with a Samco PC3000. The etch conditions are 10 sccm O_2 at 75 mTorr at 100 W for 2 min. We then pattern and e-beam evaporate Ni/Au (5 nm/40 nm) source and drain contacts (Ni being in contact with the TMD). The channel definition is done before the contact deposition to anchor the WS_2 to the substrate during the strain measurements, as Ni has high adhesion energy to Al_2O_3 compared to Au alone.[3] Lastly, we encapsulate the WS_2 transistors with an AlO_x (10 nm) layer similar to McClellan *et al.*[4] at 130 °C, which anneals and passivates the chiplet.

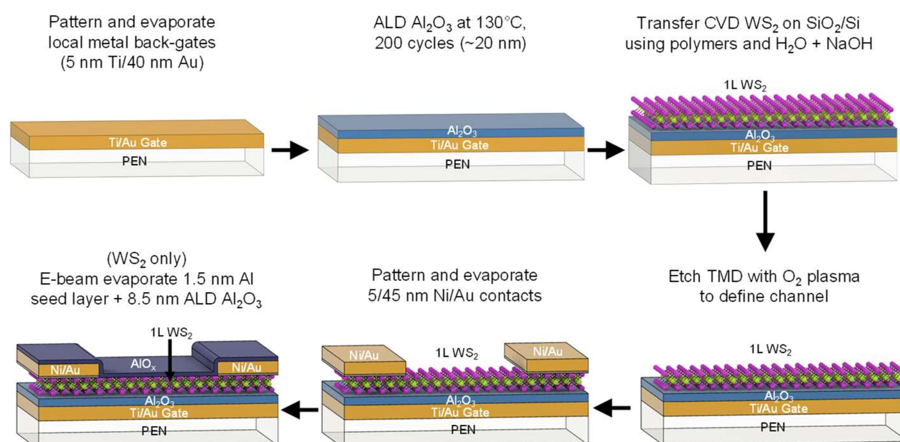

Figure S1. Summary of fabrication steps for WS_2 transistors on bendable PEN substrates. The fabrication of MoS2 transistors on PEN is identical, except for the final AlO_x encapsulation.

We acquired a 3 mm thick polymethylmethacrylate (PMMA) cross custom-machined with computer numerical control (CNC) milling and annealed the cross for 30 min at 80 °C in an oven. Compared to laser cutting, CNC milling and annealing produced PMMA crosses that could tolerate greater than 1% strain without cracking. We attached the sample to the cross with commercial cyanoacrylate (Loctite), as shown in **Figure S2a**, and mounted the cross to the biaxial strain tool (**Figure S2b**).

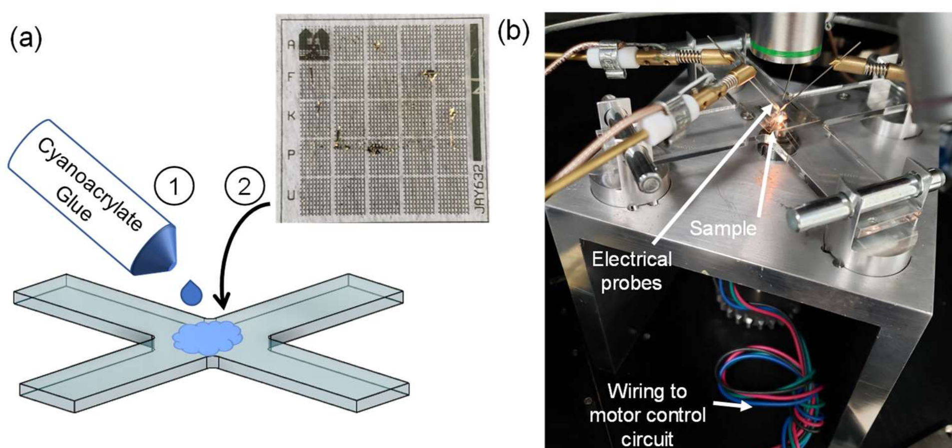

Figure S2. Sample attachment and mounting. (a) Sample attachment process with image of the PEN chiplet of 2×2 cm[2] size. Each chiplet has 5×5 (= 24 reticles plus a cat logo in the top-left corner) with 9×9 (=81) transistors each. (b) Biaxial strain tool with mounted sample on the cross under the microscope in the electrical probe station. The sample, electrical probes, and wiring to the motor control circuit are labeled. The acrylic cross is 3 mm thick, and its two arms are 115 mm long, from tip-to-tip.

2. Effect of sub-stoichiometric AlO_x encapsulation on WS_2 devices

Figure S3 shows the I_D-V_{GS} curves measured in air for 100 devices on the chiplet before and after AlO_x encapsulation. Prior to encapsulation, many devices exhibited low current and significant hysteresis. This occurs because oxygen adsorption removes electrons from the WS_2 channel, shifting the V_T positively, while charge trapping in the adsorbed molecules leads to large hysteresis in air ambient.[5,6] After encapsulation, the devices showed significant qualitative improvement. It appears that the encapsulation may passivate, electron dope,[4] as well as impart residual stress[7] into the WS_2 channel, improving the device performance and reducing device variability.

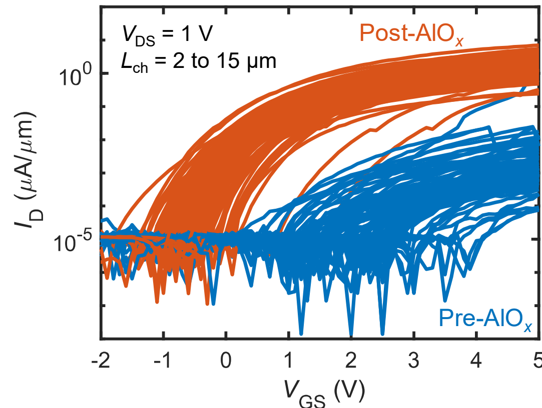

Figure S3. Measured I_D-V_{GS} curves for 100 devices showing forward sweeps of the devices before (blue) and after (red) AlO_x encapsulation at V_{DS} = 1 V for L_{ch} = 2 to 15 μm.

3. Raman and photoluminescence spectroscopy of WS_2 devices with strain

3.1 Peak fitting procedures

To track the appropriate peaks in the Raman and photoluminescence (PL) spectra of the WS_2 device channels, we fit the Raman and PL peaks using an iterative least-squares method implemented in MATLAB.[8] All Raman spectra were taken between ~100 cm^{-1} and ~550 cm^{-1}, and all PL spectra were taken between 1.7 eV and 2.1 eV. The baselines of the spectra were subtracted prior to fitting. For the Raman spectra of unencapsulated devices, four peaks were used to fit the spectral region between 300 cm^{-1} and 400 cm^{-1}, and one peak was used for the A_1' phonon mode between 400 cm^{-1} and 440 cm^{-1}. For the Raman spectra of encapsulated devices, only three peaks were used to fit the spectral region between 300 cm^{-1} and 400 cm^{-1} because the four-peak fit resulted in greater residual error. For the PL spectra of all devices, two peaks were used to fit the PL spectrum between 1.7 eV and 2.1 eV. We used an equally-weighted Gaussian-Lorentzian line shape for all peaks. The black lines in **Figure 2a and 2c** indicate the peaks used to fit the spectra.

3.2 Strain-dependent measurements of unencapsulated WS_2 devices

We measure the strain-induced peak shift rates for unencapsulated WS_2 devices to confirm that the biaxial strain tool imparts tensile strain to the TMD samples. **Figure S5** shows the Raman and PL spectra, as well as the extracted strain rates, for a single device on a second WS_2 sample prepared during the same fabrication run. Error bars for the extracted strain rates are calculated with a 95% confidence interval. While the data show large error bars because the E' and 2LA(M) modes are broad

and only ~4 cm^{-1} apart and are difficult to distinguish with certainty using least-squares methods,[9] our estimated strain rates for the device match previous literature using a similar biaxial strain mechanism.[10] Comparing **Figure S4** (unencapsulated) with **Figure 2** in the main text (encapsulated with AlO_x) we note some effects of the AlO_x encapsulation step, which removes surface oxygen and water adsorbates, inducing partial electron doping in WS_2. The encapsulation step also leads to more consistent optical measurements (**Figure 2**) during the long biaxial strain measurement sessions (several hours).

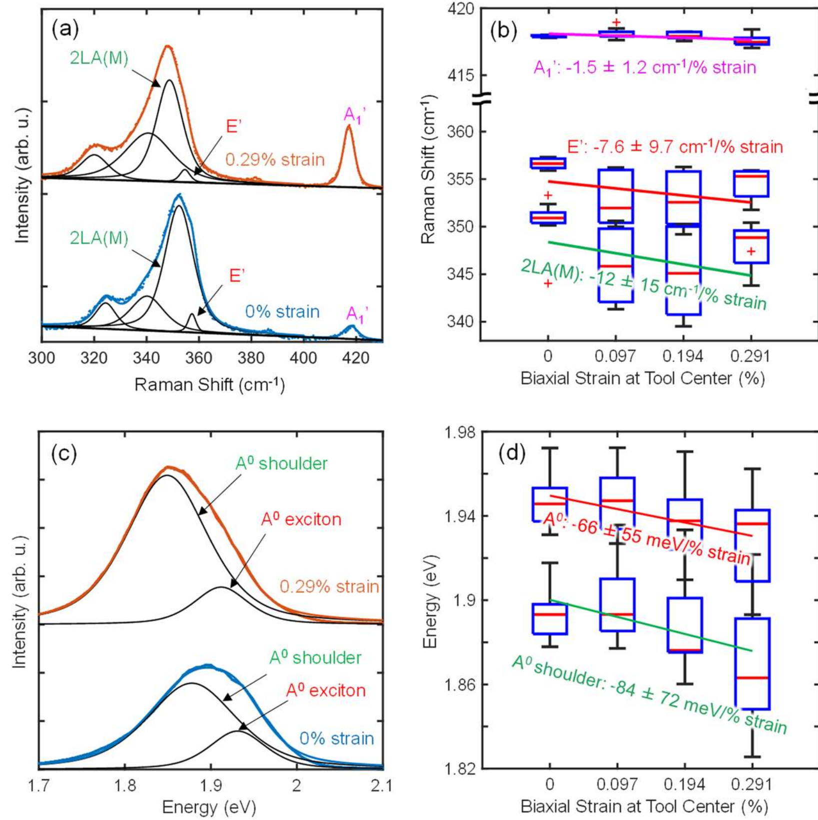

Figure S4. Strain-dependent Raman and PL measurements of an unencapsulated WS_2 device. (a) Raman spectra of a device with similar geometry as **Figure 1b** in the main text without biaxial strain (blue) and with biaxial strain applied (orange). (b) Extracted phonon shift rates of the A_1' (pink), E' (red), and 2LA(M) (green) Raman peaks of the unencapsulated WS_2 as a function of biaxial strain applied, with box plots indicating the median (red line), first, and third quartiles (blue box) across nine measured locations in the device channel. Red plus '+' symbols indicate outliers. The large error bars for the E' and 2LA(M) peaks are due to their proximity to each other (~4 cm^{-1}) and the significantly higher intensity of the 2LA(M) peak compared to the E' peak, making them difficult to distinguish using iterative computational peak fitting methods.[9] (c) PL spectra of the device at the same locations in the channel, under the same conditions and color labeling as in (a). (d) Extracted exciton shift rates of the A^0 exciton (red) and its left shoulder peak (green), with similar notation and same number of points as in (b).

4. Threshold voltage (V_T), on-current (I_{on}), and mobility (μ_{FE}) estimates

For all data reported in the main text, we estimate the threshold voltage (V_T) of our devices using the constant-current method[11] with threshold current I_T = 10 nA/µm based on the International Roadmap for Devices and Systems (IRDS) 2022 threshold for high-performance devices.[12] When this threshold

current was captured between two measured drain current (I_D) values, we used logarithmic interpolation to estimate the $V_{GS} = V_T$ at which the device would have $I_D = 10$ nA/µm.

We set the gate overdrive $V_{GS} - V_T = 5$ V to the largest integer voltage such that I_{on} and μ_{FE} could be extracted for all devices. When $V_{GS} = V_T + 5$ V falls between two instrument-measured values we use linear interpolation to estimate the $I_{on} = I_D$ at that point. At the same V_{GS} we also estimate μ_{FE} as:

$$\mu_{FE} = \frac{g_m L_{ch}}{W C_{ox} V_{DS}} = \left(\frac{\partial I_D}{\partial V_{GS}}\right)\frac{L_{ch}}{W C_{ox} V_{DS}}.$$

Although we use V_T from the constant-current[11] method throughout the main text, we also compare it with V_T from linear extrapolation[11] and Y-function[13] methods for both WS_2 and MoS_2 in **Figure S5**.

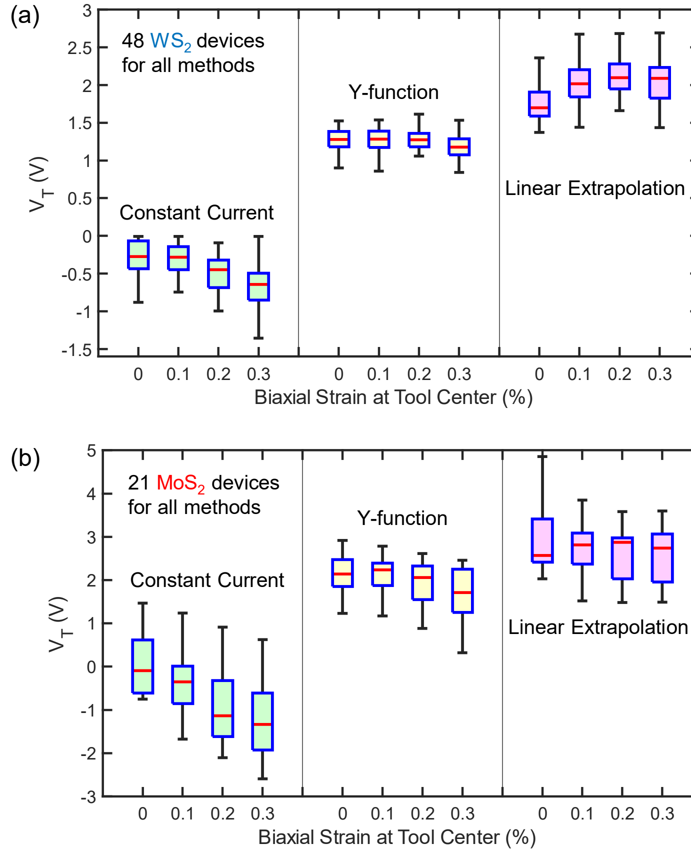

Figure S5. Comparison of V_T extraction methods for constant current (left), Y-function (middle), and linear extrapolation (right) for the (a) 48 WS_2 devices and (b) 21 MoS_2 devices. V_T is reported as a function of applied biaxial strain, from 0% (unstrained) to 0.3%.

In **Figure S5**, we note that threshold voltages are generally around zero for our devices, but there are several discrepancies between V_T extracted from various methods. These have been previously observed in the TMD device literature[1,14] and they are due to at least two causes: 1) the constant-current V_T is somewhat arbitrary, and a larger V_T can be extracted if this is done at a larger current, *e.g.* I_D = 100 nA/µm, and 2) the measured I_D-V_{GS} curves (on linear axes) often display a "round knee" at lower V_{GS}, before reaching the true linear region at higher V_{GS}. This is partly due to the contacts "turning on" at different V_{GS} from the channel[14–16] and partly due to more trap-assisted (hopping) transport at lower

V_{GS}, closer to threshold.[17,18] Hence, we report all our data (for I_{on} and μ_{FE}) at "as high a V_{GS} as possible" everywhere else in our study, to be in the linear region of our devices.

We recall that in the main text (**Figures 3c,d** and **4c,d**), we reported all our findings at $V_{GS} - V_T = 5$ V, which was the highest V_{GS} in the linear region for a substantial number of devices (48 for WS_2 and 21 for MoS_2). For comparison, in **Figure S6**, we also report the I_{on} and μ_{FE} at a lower $V_{GS} - V_T = 4$ V, which now includes 60 WS_2 and 20 MoS_2 devices. Overall, the improvements with applied biaxial strain are slightly lower than those at $V_{GS} - V_T = 5$ V reported in the main text. Compare, for example, **Figure S6a,b** below with **Figure 3c,d** in the main text. This suggests that strain-induced device improvements may be slightly better at higher gate overdrive, potentially due to better contact gating (and reduced contact resistance) at higher V_{GS}. However, there is sufficient uncertainty in the average I_{on} improvement (*e.g.* 1.8 ± 0.5 times at 0.3% strain, see **Figure 3c**) that its root cause remains unclear, and it will be the subject of future studies.

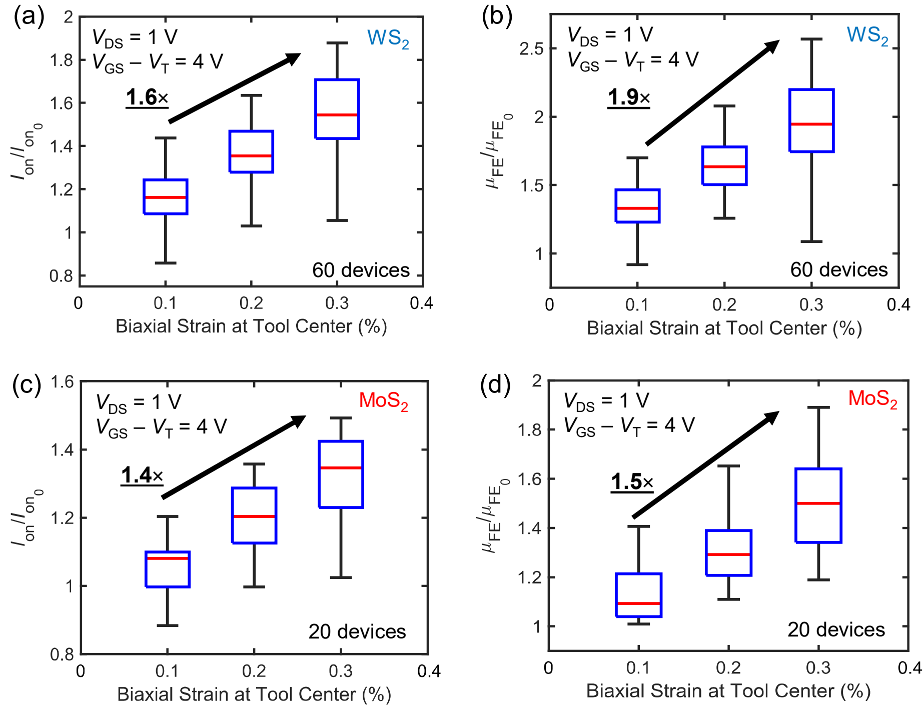

Figure S6. Box plots of normalized I_{on} and μ_{FE} improvement as a function of applied biaxial tensile strain similar to **Figures 3c,d** and **4c,d** in the main text, extracted at $V_{DS} = 1$ V and $V_{GS} - V_T = 4$ V. (a-b) display relative I_{on} and μ_{FE} changes across 60 WS_2 devices and (c-d) are across 20 MoS_2 devices. The I_{on} and μ_{FE} improve by 1.6 ± 0.14 and 1.9 ± 0.19 respectively for WS_2, and 1.4 ± 0.25 and 1.5 ± 0.40 respectively for MoS_2 devices. For comparison, those in the main text figures are at a larger gate overdrive, $V_{GS} - V_T = 5$ V.

5. Current-voltage characteristics of TMD transistors with strain

We measure our devices electrically with a Keithley 4200-SCS using Keithley Interactive Test Environment (KITE) software. **Figure S7** displays the same I_D-V_{GS} curves for the devices in **Figures 3a** and **4a** of the main text, but here includes the reverse sweep (dashed lines) and gate current (dotted lines) with the forward sweep (solid lines). The mismatched forward and backward sweeps point to hysteresis in the devices, likely arising from electrically active interfacial traps between the TMD and Al_2O_3 due to adsorbates from the transfer process.[19] The gate current (I_G) remains at or below the tool

measurement threshold (~100 pA) throughout all four WS_2 measurements, indicating no substantial leakage current through the gate dielectric. The Keithley 4200-SCS settings were later adjusted to measure lower gate currents more accurately for the MoS_2 transistors.

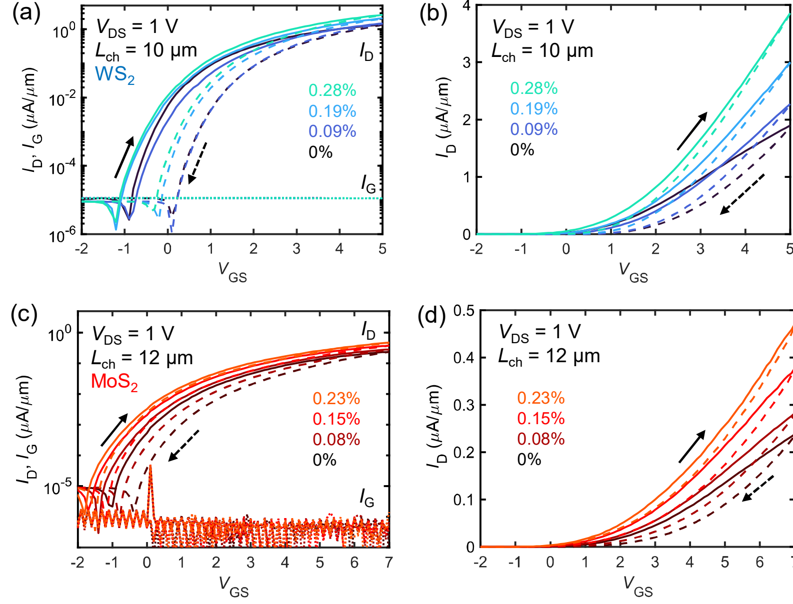

Figure S7. (a-b) Measured I_D-V_{GS} curves showing forward (solid) and backward (dashed lines) sweeps at different strain levels for the same WS_2 device (a-b) shown in **Figure 3a** of the main text, with W = 20 μm, L_{ch} = 10 μm, and V_{DS} = 1 V, on (a) logarithmic scale and (b) linear scale. The gate current (I_G) is below the tool measurement range setting (~100 pA). (c-d) Measured I_D-V_{GS} for the MoS_2 device from **Figure 4a** of the main text, with W = 20 μm, L_{ch} = 12 μm, and V_{DS} = 1 V. The gate current, I_G, is also normalized by the channel width, like the drain current.

Figure S8 plots the hysteresis (defined as the difference in V_T between the reverse and forward sweeps divided by the voltage sweep range) vs. strain for the 48 WS_2 devices included in **Figure 3c-d** and the 21 MoS_2 devices in **Figure 4c-d**. We observe negligible dependence of hysteresis on strain, within the range applied here, for our devices.

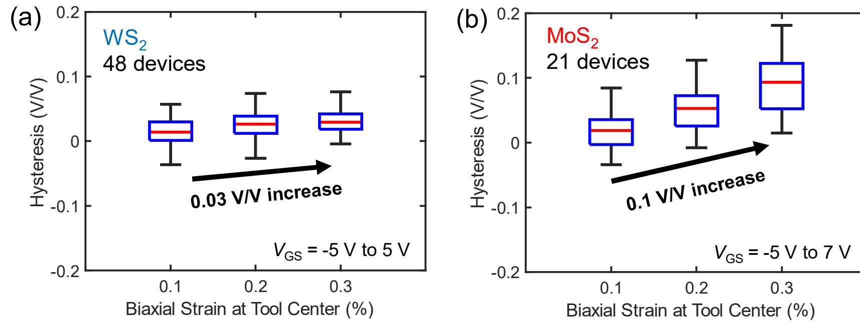

Figure S8. Box plots showing extracted hysteresis values for (a) 48 WS_2 devices, and (b) 21 MoS_2 devices as a function of biaxial tensile strain. The hysteresis is computed as the ratio of ($V_{T,reverse} - V_{T,forward}$) divided by the voltage sweep range (here, 10 V for WS_2 and 12 V for MoS_2, although only the ranges of interest are shown in **Figure S7**).

6. WS_2 devices at high biaxial strain and after strain relaxation

We measured the WS_2 devices at 0.4% applied biaxial strain and after strain relaxation. (Similar measurements for uniaxially strained and relaxed MoS_2 devices on flexible substrates were carried out by Datye *et al.*[20]) The relaxed measurement was completed several days after the initial strain measurement to ensure that residual creep strain in the acrylic cross had fully relaxed.

Figure S9 shows one device at 0.4% applied biaxial strain and after strain relaxation. The device exhibited poorer I_D at 0.4% strain and gate leakage after relaxation. The lower I_D suggests poorer contact adhesion at high strain, and the increased gate leakage (I_G) indicates that the Al_2O_3 gate dielectric likely suffered mechanical defects under the shear strains imparted by the tool.

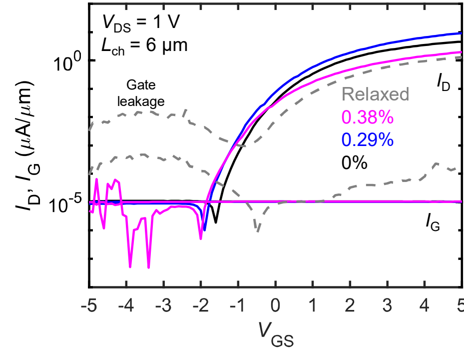

Figure S9. Measured drain (I_D) and gate (I_G) current vs. V_{GS} at different strain levels for a device with W = 20 µm, L_{ch} = 6 µm, and V_{DS} = 1 V. Black, blue, magenta, and gray correspond to 0%, 0.29%, 0.38% strain (solid lines) and after strain relaxation (dashed lines), respectively.

Figure S10 shows the box plots of I_{on} and μ_{FE} for the 8 working devices that survived the higher-strain (up to 0.4%) and return to a relaxed state. While up to 0.3% strain the trend is clear, at 0.4% strain over 75% of the 48 measured devices either exhibited shorted gate-to-contact behavior or showed significant current degradation. The shorted gate indicates that the strain likely caused microcracks in the Al_2O_3 that further broke down under electrical stress.[21] In addition, the current degradation occurred likely due to slippage at the WS_2-contact interfaces.[20] After relaxation, the surviving devices (on average) return to their original (unstrained) I_{on} and μ_{FE}, albeit with a broader distribution due to the devices that exhibited partial failure (note the lower bar of the box plot near the bottom axis).

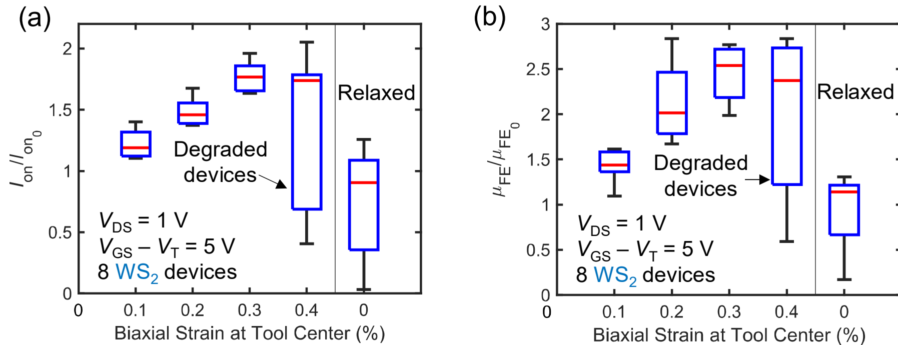

Figure S10. Box plots of the normalized (a) I_{on} and (b) μ_{FE} for the remaining 8 devices whose V_T could be extracted after the strain measurements. Three of the devices showed significant degradation at 0.4% strain, creating the large spread of the box plot, while the other five largely returned to their original I_{on} and μ_{FE} after relaxation.

We note that the surviving devices were located ~3 mm away from the tool center and likely did not experience more than 70% of the applied biaxial strain at the tool center, as discussed the subsequent section and in the finite-element simulations performed by Michail *et al.*[22] At 0.4% applied biaxial strain at the tool center, these devices would have experienced ~0.28% strain, thus not exceeding the breaking point.

7. Strain fields induced by biaxial strain tool

Because the deflection occurs at the center of the cross, the strain field in the sample for each strain level is approximately radial with the maximum strain at the center of the tool.[22] **Figure S11** shows the spatial distribution of measured devices for each strain level on the WS_2 sample, with the colors indicating the improvements in mobility, relative to the unstrained case. Devices near the center of the tool appear to have larger improvements from 0.1%-0.3% strain and degrade at 0.4% strain.[22]

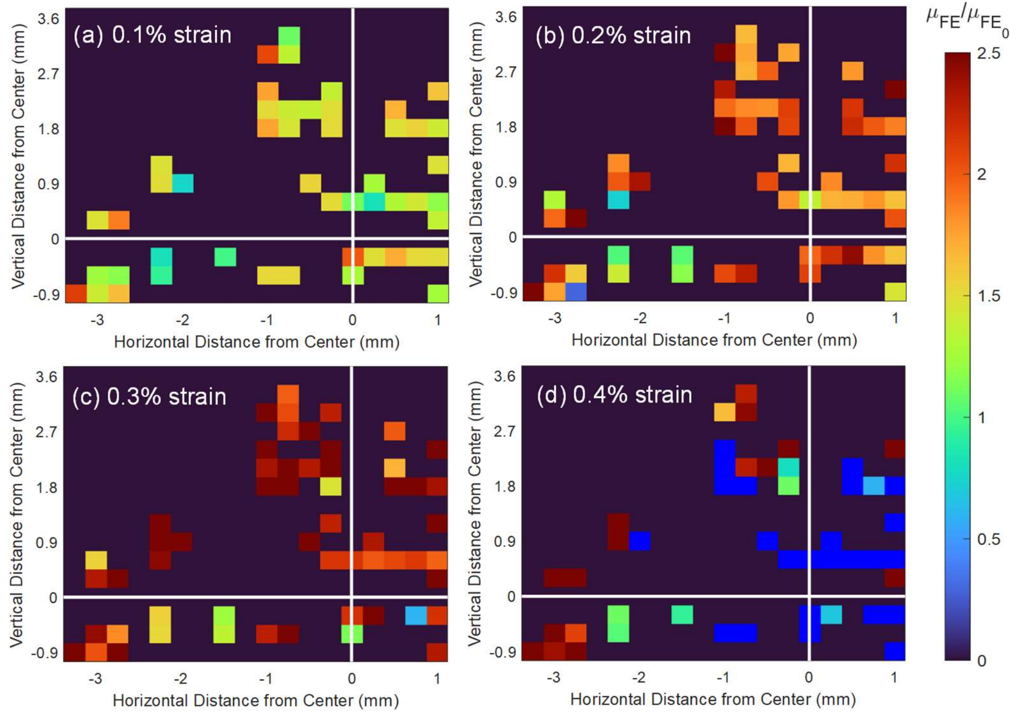

Figure S11. Heat maps showing the spatial distribution of the devices across the sample relative to the center of the strain tool and their corresponding μ_{FE} (normalized with respect to the unstrained devices). (a) At 0.1% applied biaxial tensile strain, (b) at 0.2%, (c) at 0.3%, (d) at 0.4%. On average, mobility improves from 0.1% to 0.3% applied strain. At 0.4%, devices near the center of the cross begin to degrade, as seen by the sharp drop of mobility (blue tiles). Dark blue tiles in panel (d) represent devices whose mobilities could not be extracted. Only a subset of the functioning fabricated devices (48 colored "tiles" in each panel) were measured here.

8. Density functional theory (DFT) simulations of strained WS_2 band structure

We employ DFT calculations with spin-orbit coupling to understand the causes of mobility enhancement in our biaxially-strained devices. We calculate the band structure for WS_2 under no strain and from 0.1% to 1% uniaxial and biaxial strain. **Figure S12** shows the calculated band structure relative to the conduction band edge, and the reduction of the energy band gap (E_G) with tensile strain. We observe a ~40 meV shift in V_T with 0.3% biaxial tensile strain applied in this study, which is small

compared to our gate voltage overdrive used for mobility extraction. We also note that the calculated reduction of E_G by -128 ± 0.41 meV/% biaxial tensile strain closely matches the measured A^0 exciton shift rate in the PL spectra of **Figure 2(c,d)**.

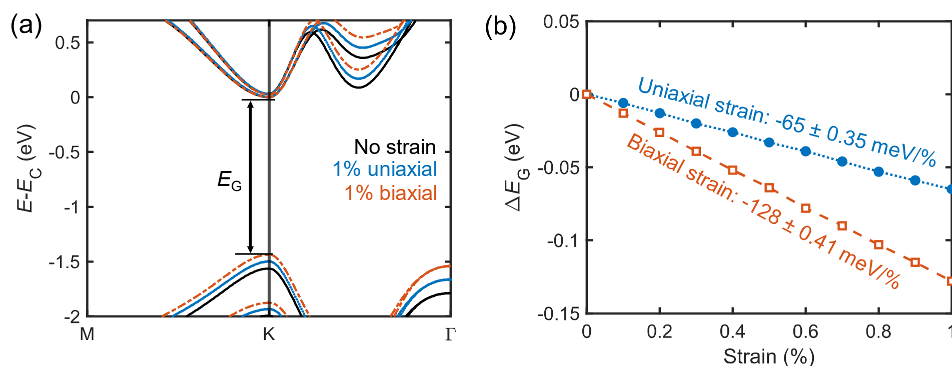

Figure S12. DFT calculations with spin-orbit coupling. (a) Calculated band structure of WS_2 with no strain (black solid line), 1% uniaxial tensile strain (blue solid line), and 1% biaxial tensile strain (orange dotted-dashed line) relative to the conduction band edge. (b) Calculated energy band gap reduction (ΔE_G) for uniaxial (blue dotted line) and biaxial (orange dashed line) tensile strain from 0% to 1%. Markers indicate calculated points.

9. Channel length dependence of strain-induced mobility improvements

To confirm that the strain-induced improvement of mobility is not a contact effect, we plot the mobility improvement against channel length in **Figure S13**. We observe that the device variability within each channel length is greater than the variation across channel lengths, indicating that the local channel material quality dominates over contact effects in our data.

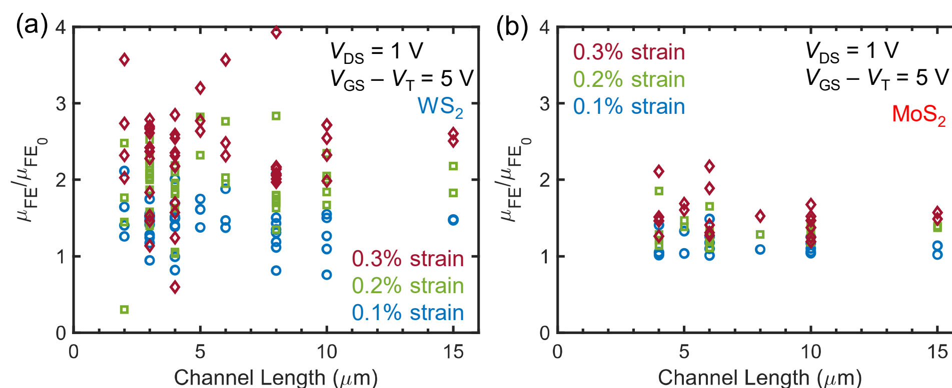

Figure S13. Channel length dependence of strain-induced mobility improvement in (a) WS_2 and (b) MoS_2 transistors. Each symbol represents one device measured at one strain point, with blue circles representing 0.1% biaxial tensile strain, green squares representing 0.2% strain, and red diamonds representing 0.3% strain. Mobilities are estimated at a gate voltage overdrive of 5 V with constant-current V_T.

10. Supplementary References

(1) Smithe, K. K. H.; Suryavanshi, S. V.; Muñoz Rojo, M.; Tedjarati, A. D.; Pop, E. Low Variability in Synthetic Monolayer MoS2 Devices. *ACS Nano* **2017**, *11* (8), 8456–8463. https://doi.org/10.1021/acsnano.7b04100.

(2) Vaziri, S.; Yalon, E.; Muñoz Rojo, M.; Suryavanshi, S. V.; Zhang, H.; McClellan, C. J.; Bailey, C. S.; Smithe, K. K. H.; Gabourie, A. J.; Chen, V.; Deshmukh, S.; Bendersky, L.; Davydov, A. V.; Pop, E. Ultrahigh Thermal Isolation across Heterogeneously Layered Two-Dimensional Materials. *Sci. Adv.* **2021**, *5* (8), eaax1325. https://doi.org/10.1126/sciadv.aax1325.

(3) Li, H.-T.; Chen, L.-F.; Yuan, X.; Zhang, W.-Q.; Smith, J. R.; Evans, A. G. Interfacial Stoichiometry and Adhesion at Metal/α-Al2O3 Interfaces. *J. Am. Ceram. Soc.* **2011**, *94* (s1), s154–s159. https://doi.org/10.1111/j.1551-2916.2011.04405.x.

(4) McClellan, C. J.; Yalon, E.; Smithe, K. K. H.; Suryavanshi, S. V.; Pop, E. High Current Density in Monolayer MoS_2 Doped by AlO_x. *ACS Nano* **2021**, *15* (1), 1587–1596. https://doi.org/10.1021/acsnano.0c09078.

(5) Liang, Q.; Gou, J.; Arramel; Zhang, Q.; Zhang, W.; Wee, A. T. S. Oxygen-Induced Controllable p-Type Doping in 2D Semiconductor Transition Metal Dichalcogenides. *Nano Res.* **2020**, *13* (12), 3439–3444. https://doi.org/10.1007/s12274-020-3038-8.

(6) Urban, F.; Giubileo, F.; Grillo, A.; Iemmo, L.; Luongo, G.; Passacantando, M.; Foller, T.; Madauß, L.; Pollmann, E.; Geller, M. P.; Oing, D.; Schleberger, M.; Bartolomeo, A. D. Gas Dependent Hysteresis in MoS_2 Field Effect Transistors. *2D Mater.* **2019**, *6* (4), 045049. https://doi.org/10.1088/2053-1583/ab4020.

(7) Ylivaara, O. M. E.; Liu, X.; Kilpi, L.; Lyytinen, J.; Schneider, D.; Laitinen, M.; Julin, J.; Ali, S.; Sintonen, S.; Berdova, M.; Haimi, E.; Sajavaara, T.; Ronkainen, H.; Lipsanen, H.; Koskinen, J.; Hannula, S.-P.; Puurunen, R. L. Aluminum Oxide from Trimethylaluminum and Water by Atomic Layer Deposition: The Temperature Dependence of Residual Stress, Elastic Modulus, Hardness and Adhesion. *Thin Solid Films* **2014**, *552*, 124–135. https://doi.org/10.1016/j.tsf.2013.11.112.

(8) O'Haver, T. Interactive Peak Fitter, 2021. https://terpconnect.umd.edu/~toh/spectrum/InteractivePeakFitter.htm.

(9) McCreary, A.; Berkdemir, A.; Wang, J.; Nguyen, M. A.; Elías, A. L.; Perea-López, N.; Fujisawa, K.; Kabius, B.; Carozo, V.; Cullen, D. A.; Mallouk, T. E.; Zhu, J.; Terrones, M. Distinct Photoluminescence and Raman Spectroscopy Signatures for Identifying Highly Crystalline WS_2 Monolayers Produced by Different Growth Methods. *J. Mater. Res.* **2016**, *31* (7), 931–944. https://doi.org/10.1557/jmr.2016.47.

(10) Michail, A.; Anestopoulos, D.; Delikoukos, N.; Grammatikopoulos, S.; Tsirkas, S. A.; Lathiotakis, N. N.; Frank, O.; Filintoglou, K.; Parthenios, J.; Papagelis, K. Tuning the Photoluminescence and Raman Response of Single-Layer WS_2 Crystals Using Biaxial Strain. *J. Phys. Chem. C* **2023**, *127* (7), 3506–3515. https://doi.org/10.1021/acs.jpcc.2c06933.

(11) Ortiz-Conde, A.; García Sánchez, F. J.; Liou, J. J.; Cerdeira, A.; Estrada, M.; Yue, Y. A Review of Recent MOSFET Threshold Voltage Extraction Methods. *Microelectron. Reliab.* **2002**, *42* (4), 583–596. https://doi.org/10.1016/S0026-2714(02)00027-6.

(12) *International Roadmap for Devices and Systems 2022*; Institute of Electrical and Electronics Engineers, 2022. https://irds.ieee.org/editions/2022 (accessed 2023-07-07).

(13) Pacheco-Sanchez, A.; Jiménez, D. Accuracy of Y -Function Methods for Parameters Extraction of Two-Dimensional FETs across Different Technologies. *Electron. Lett.* **2020**, *56* (18), 942–945. https://doi.org/10.1049/el.2020.1502.

(14) Sebastian, A.; Pendurthi, R.; Choudhury, T. H.; Redwing, J. M.; Das, S. Benchmarking Monolayer MoS_2 and WS_2 Field-Effect Transistors. *Nat. Commun.* **2021**, *12* (1), 693. https://doi.org/10.1038/s41467-020-20732-w.
(15) Pang, C.-S.; Zhou, R.; Liu, X.; Wu, P.; Hung, T. Y. T.; Guo, S.; Zaghloul, M. E.; Krylyuk, S.; Davydov, A. V.; Appenzeller, J.; Chen, Z. Mobility Extraction in 2D Transition Metal Dichalcogenide Devices—Avoiding Contact Resistance Implicated Overestimation. *Small* **2021**, *17* (28), 2100940. https://doi.org/10.1002/smll.202100940.
(16) Arutchelvan, G.; Smets, Q.; Verreck, D.; Ahmed, Z.; Gaur, A.; Sutar, S.; Jussot, J.; Groven, B.; Heyns, M.; Lin, D.; Asselberghs, I.; Radu, I. Impact of Device Scaling on the Electrical Properties of MoS_2 Field-Effect Transistors. *Sci. Rep.* **2021**, *11* (1), 6610. https://doi.org/10.1038/s41598-021-85968-y.
(17) Wang, L.; Li, Y.; Gong, X.; Thean, A. V.-Y.; Liang, G. A Physics-Based Compact Model for Transition-Metal Dichalcogenides Transistors With the Band-Tail Effect. *IEEE Electron Device Lett.* **2018**, *39* (5), 761–764. https://doi.org/10.1109/LED.2018.2820142.
(18) Zhu, W.; Low, T.; Lee, Y.-H.; Wang, H.; Farmer, D. B.; Kong, J.; Xia, F.; Avouris, P. Electronic Transport and Device Prospects of Monolayer Molybdenum Disulphide Grown by Chemical Vapour Deposition. *Nat. Commun.* **2014**, *5* (1), 3087. https://doi.org/10.1038/ncomms4087.
(19) Datye, I. M.; Gabourie, A. J.; English, C. D.; Smithe, K. K. H.; McClellan, C. J.; Wang, N. C.; Pop, E. Reduction of Hysteresis in MoS_2 Transistors Using Pulsed Voltage Measurements. *2D Mater.* **2019**, *6* (1), 011004. https://doi.org/10.1088/2053-1583/aae6a1.
(20) Datye, I. M.; Daus, A.; Grady, R. W.; Brenner, K.; Vaziri, S.; Pop, E. Strain-Enhanced Mobility of Monolayer MoS_2. *Nano Lett.* **2022**, *22* (20), 8052–8059. https://doi.org/10.1021/acs.nanolett.2c01707.
(21) Chang, H.-Y.; Yang, S.; Lee, J.; Tao, L.; Hwang, W.-S.; Jena, D.; Lu, N.; Akinwande, D. High-Performance, Highly Bendable MoS_2 Transistors with High-K Dielectrics for Flexible Low-Power Systems. *ACS Nano* **2013**, *7* (6), 5446–5452. https://doi.org/10.1021/nn401429w.
(22) Michail, A.; Anestopoulos, D.; Delikoukos, N.; Parthenios, J.; Grammatikopoulos, S.; Tsirkas, S. A.; Lathiotakis, N. N.; Frank, O.; Filintoglou, K.; Papagelis, K. Biaxial Strain Engineering of CVD and Exfoliated Single- and Bi-Layer MoS_2 Crystals. *2D Mater.* **2020**, *8* (1), 015023. https://doi.org/10.1088/2053-1583/abc2de.